

Observations of 6.7 GHz methanol masers with East-Asian VLBI Network. I. VLBI images of the first epoch of observations

Kenta FUJISAWA,^{1,2,*} Koichiro SUGIYAMA,² Kazuhito MOTOGI,²
Kazuya HACHISUKA,³ Yoshinori YONEKURA,⁴ Satoko SAWADA-SATOH,⁵
Naoko MATSUMOTO,⁶ Kazuo SORAI,⁷ Munetake MOMOSE,⁸ Yu SAITO,⁸
Hiroshi TAKABA,⁹ Hideo OGAWA,¹⁰ Kimihiro KIMURA,¹⁰ Kotaro NIINUMA,²
Daiki HIRANO,² Toshihiro OMODAKA,¹¹ Hideyuki KOBAYASHI,⁶
Noriyuki KAWAGUCHI,⁶ Katsunori M. SHIBATA,⁶ Mareki HONMA,⁶
Tomoya HIROTA,⁶ Yasuhiro MURATA,^{12,13} Akihiro DOI,^{12,13}
Nanako MOCHIZUKI,¹² Zhiqiang SHEN,^{3,14} Xi CHEN,^{3,14} Bo XIA,^{3,14}
Bin LI,^{3,14} and Kee-Tae KIM¹⁵

¹The Research Institute for Time Studies, Yamaguchi University, 1677-1 Yoshida, Yamaguchi, Yamaguchi, JP 753-8511

²Graduate School of Science and Engineering, Yamaguchi University, 1677-1 Yoshida, Yamaguchi, Yamaguchi 753-8512

³Shanghai Astronomical Observatory, Chinese Academy of Sciences, 80 Nandan Road, Shanghai 200030 China

⁴Center for Astronomy, Ibaraki University, 2-1-1 Bunkyo, Mito, Ibaraki 310-8512

⁵Mizusawa VLBI Observatory, National Astronomical Observatory of Japan (NAOJ), 2-12 Hoshigaoka-cho, Mizusawa-ku, Oshu, Iwate 023-0861

⁶Mizusawa VLBI Observatory, National Astronomical Observatory of Japan (NAOJ), 2-21-1 Osawa, Mitaka, Tokyo 181-8588

⁷Department of Physics / Department of Cosmosciences, Hokkaido University, Kita 10, Nishi 8, Kita-ku, Sapporo 060-0810

⁸College of Science, Ibaraki University, 2-1-1 Bunkyo, Mito, Ibaraki 310-8512

⁹Faculty of Engineering, Gifu University, 1-1 Yanagido, Gifu, Gifu 501-1193

¹⁰Department of Physical Science, Osaka Prefecture University, 1-1 Gakuen-cho, Naka-ku, Sakai Osaka 599-8531

¹¹Department of Physics and Astronomy, Graduate School of Science and Engineering, Kagoshima University, 1-21-35 Korimoto, Kagoshima, Kagoshima 890-0065

¹²Institute of Space and Astronautical Science, Japan Aerospace Exploration Agency, 3-1-1 Yoshinodai, Chuou-ku, Sagamihara 229-8510

¹³Department of Space and Astronautical Science, The Graduate University for Advanced Studies, 3-1-1 Yoshinodai, Chuou-ku, Sagamihara 229-8510

¹⁴Key Laboratory of Radio Astronomy, Chinese Academy of Sciences, 2 West Beijing Road, 210008, Nanjing, China

¹⁵Korea Astronomy and Space Science Institute, 776 Daedeokdae-ro, Yuseong-gu, Daejeon 305-348, Republic of Korea

*E-mail: kenta@yamaguchi-u.ac.jp

Received 2013 July 30; Accepted 2013 October 29

© The Author 2014. Published by Oxford University Press on behalf of the Astronomical Society of Japan.
All rights reserved. For Permissions, please email: journals.permissions@oup.com

Abstract

Very-long-baseline interferometry (VLBI) monitoring of the 6.7 GHz methanol maser allows us to measure the internal proper motion of maser spots and therefore study the gas motion around high-mass young stellar objects. To this end, we have begun monitoring observations with the East-Asian VLBI Network. In this paper we present the results of the first epoch observation for 36 sources, including 35 VLBI images of the methanol maser. Since two independent sources were found in three images, images of 38 sources were obtained. In 34 sources, 10 or more spots were detected. The observed spatial scale of the maser distribution was from 9 to 4900 astronomical units, and the following morphological categories were observed: elliptical, arched, linear, paired, and complex. The position of the maser spot was determined with an accuracy of approximately 0.1 mas, which is sufficiently high to measure the internal proper motion from two years of monitoring observations. The VLBI observation, however, detected only approximately 20% of all maser emissions, suggesting that the remaining 80% of the total flux was spread into an undetectable extended distribution. Therefore, in addition to high-resolution observations, it is important to observe the whole structure of the maser emission including extended low-brightness structures, in order to reveal the associated site of the maser and gas motion.

Key words: H II regions — instrumentation: high angular resolution — masers — stars: formation

1 Introduction

Although high-mass star formation has been intensively studied, it remains poorly understood because of the large distance and high obscuration of the high-mass star-forming regions and the short duration of critical evolutionary phases (Zinnecker & Yorke 2007 and references therein). Star-forming regions are associated with maser emissions of high brightness temperature and high transparency in the radio band, which are suitable for probing young stellar objects (YSOs). Maser emissions are particularly useful for tracing circumstellar gas motions close to the central star. The 6.7 GHz methanol maser transition, which is the brightest among the methanol masers, is observed only in high-mass star-forming regions (e.g., Menten 1991; Caswell et al. 1995; Minier et al. 2003; Xu et al. 2008) and considered to be one of the best tracers of gas dynamics around high-mass YSOs.

Some 6.7 GHz methanol masers show linearly elongated morphology with a linear velocity gradient (Norris et al. 1993; Phillips et al. 1998; Walsh et al. 1998; Minier et al. 2000). These masers can be interpreted as a circumstellar disk viewed edge-on. Bartkiewicz et al. (2009) analyzed selected sources by using very-long-baseline interferometry (VLBI) imaging observed through the European VLBI Network (EVN). They found elliptical morphology in 30% of the sampled methanol masers and deduced that this morphology arises from inclined rotating disks with expansion or infall motion. In fact, rotational motions consistent with circumstellar disks have been identified as internal

proper motions in a few 6.7 GHz methanol maser sources (G16.59–0.05, G23.01–0.41, and IRAS 20126+4104; Sanna et al. 2010a, 2010b; Moscadelli et al. 2011). In addition, the 6.7 GHz methanol maser source AFGL 5142 exhibits an infall proper motion (Goddi et al. 2011), while a rotation and infall motion are observed in Cepheus A (Sugiyama et al. 2014).

On the other hand, the sites associated with 6.7 GHz methanol masers remain obscure. De Buizer (2003) and De Buizer et al. (2009) reported that, in 60% of their samples, the methanol maser spots were distributed along the elongated direction of the H₂ $v = 1 - 0$ S(1) at 2.12 μ m and SiO thermal line emissions, which are shock diagnostic. According to these authors, such a parallel distribution suggests that methanol masers are directly associated with outflows. Outward proper motions have been found in a few 6.7 GHz methanol maser sources (Rygl et al. 2010; Sugiyama et al. 2011; Matsumoto et al. 2011; Sawada-Satoh et al. 2013), which supports this inference. Pandian et al. (2011) observed linear/arched morphology in only nine out of 50 sources with the Multi-Element Radio-Linked Interferometric Network (MERLIN) and the Karl G. Jansky Very Large Array (JVLA), and they did not detect any source with clear elliptical morphology, in contrast to the results of Bartkiewicz et al. (2009).

If we use masers for studying high-mass star formation, the origin of the 6.7 GHz methanol maser must be elucidated. This can be achieved with VLBI monitoring of numerous unbiased sources, from which the spatial

Table 1. Summary of the 6.7 GHz methanol maser sources observed by VLBI.*

No.	G-Name	IRAS	Coordinates (J2000.0)		V_{lsr} (km s ⁻¹)	F_{p} (Jy)	D (kpc)	Reference [†]
			RA (^h ^m ^s)	Dec ([°] ['] ^{''})				
1	000.54–00.85	17470–2853	17 50 14.35	–28 54 31.1	11.8	68	7.2	cas10
2	000.64–00.04	17441–2822	17 47 18.65	–28 24 25.0	49.1	69	7.9 [‡]	cas10
3	002.53+00.19	17476–2638	17 50 46.47	–26 39 45.3	3.1	88	4.2	cas10
4	006.18–00.35		18 01 02.16	–23 47 10.8	–30.2	228.57	5.1	gre10
5	006.79–00.25	17589–2312	18 01 57.75	–23 12 34.9	16.3	91.07	3.8	gre10
6	008.68–00.36	18032–2137	18 06 23.49	–21 37 10.2	43.2	102.0	4.5	gre10
7	008.83–00.02	18024–2119	18 05 25.67	–21 19 25.1	–3.8	159.08	5.2	gre10
8	009.61+00.19	18032–2032	18 06 14.92	–20 31 44.3	5.5	70.00	5.2 [‡]	gre10
9	009.98–00.02	18048–2019	18 07 50.12	–20 18 56.5	42.2	67.58	12.0	gre10
10	010.32–00.16	18060–2005	18 09 01.46	–20 05 07.8	11.5	90.05	2.39	gre10
11	011.49–01.48	18134–1942	18 16 22.13	–19 41 27.1	6.6	68.40	1.6	gre10
12	011.90–00.14	18092–1842	18 12 11.44	–18 41 28.6	42.9	64.89	4.0	gre10
13	012.02–00.03	18090–1832	18 12 01.86	–18 31 55.7	108.3	96.26	11.1	gre10
14	012.68–00.18		18 13 54.75	–18 01 46.6	57.5	544.0	2.40 [‡]	imm13
15	012.88+00.48	18089–1732	18 11 51.40	–17 31 29.6	39.3	68.88	2.34 [‡]	gre10
16	014.10+00.08	18128–1640	18 15 45.81	–16 39 09.4	15.4	87.26	5.4	gre10
17	020.23+00.06	18249–1116	18 27 44.56	–11 14 54.2	71.8	77	4.4	cas09
18	023.43–00.18	18319–0834	18 34 39.25	–08 31 38.5	103	45	5.9 [‡]	cas09
19	025.65+01.05	18316–0602	18 34 20.91	–05 59 40.5	41.9	178	12.5	xu09
20	025.71+00.04	18353–0628	18 38 03.15	–06 24 15.0	92.8	364	11.8	xu09
21	025.82–00.17	18361–0627	18 39 03.63	–06 24 09.5	91.2	70	5.0	xu09
22	028.83–00.25	18421–0348	18 44 51.08	–03 45 48.5	83.5	73	4.6	cyg09
23	029.86–00.04		18 45 59.57	–02 45 04.4	101.4	67	9.3	xu09
24	030.70–00.06	18450–0205	18 47 36.9	–02 01 05	88	87	5.9	xu09
25	030.76–00.05	18450–0200	18 47 39.73	–01 57 22.0	92	68	4.8	xu09
26	030.91+00.14	18448–0146	18 47 15.0	–01 44 07	104	95.2	5.6	xu09
27	031.28+00.06	18456–0129	18 48 12.39	–01 26 22.6	110	71	5.8	xu09
28	032.03+00.06	18470–0049	18 49 37.3	–00 45 47	92.8	93	7.2	xu09
29	037.40+01.52	18517+0437	18 54 10.5	+04 40 49	41.1	279	2.1	xu09
30	049.49–00.38	19213+1424	19 23 43.949	+14 30 34.44	59.2	850	5.41 [‡]	xu09
31	232.62+00.99	07299–1651	07 32 09.79	–16 58 12.4	23	162	1.68 [‡]	cas09
32	351.77–00.53	17233–3606	17 26 42.57	–36 09 17.6	1.3	231	0.4	cas10
33	352.63–01.06	17278–3541	17 31 13.91	–35 44 08.7	–2.9	183	0.9	cas10
34	353.41–00.36	17271–3439	17 30 26.18	–34 41 45.6	–20.3	116	3.8	cas10
35	354.61+00.47	17269–3312	17 30 17.13	–33 13 55.1	–24.4	166	3.8	cas10
36	359.43–00.10		17 44 40.60	–29 28 16.0	–47.8	73.50	8.2	cas10

*Column 1: ID number, columns 2 and 3: Galactic and IRAS names (if any) respectively, columns 4 and 5: Absolute coordinates (referenced in column 9), columns 6 and 7: Radial velocity and peak flux density of the brightest maser feature respectively, column 8: Source distance (referenced in section 4), column 9: Absolute coordinate reference.

[†]Reference: cas09, Caswell (2009); cyg09, Cyganowski et al. (2009); xu09, Xu et al. (2009b); cas10, Caswell et al. (2010); gre10, Green et al. (2010); imm13, Immer et al. (2013).

[‡]Distances determined by trigonometric parallax.

distribution and the three-dimensional velocity field (radial velocity and proper motions in RA and Dec) of the maser can be statistically investigated.

To date, VLBI images of 6.7 GHz methanol masers have been reported on for approximately 60 sources (e.g., Minier et al. 2000; Dodson et al. 2004; Sugiyama et al. 2008; Bartkiewicz et al. 2009), while masers have been detected in more than 900 high-mass star-forming regions (Pestalozzi

et al. 2005 and references therein; Ellingsen 2007; Pandian et al. 2007; Xu et al. 2009b; Caswell et al. 2010, 2011; Green et al. 2010, 2012). As mentioned above, the internal proper motion of the 6.7 GHz methanol maser has been measured in only a small fraction of cases. Therefore, we have started a VLBI monitoring project of the 6.7 GHz methanol maser sources with the East-Asian VLBI Network (EAVN) to systematically investigate their internal

proper motions. This study presents the initial results of this project, namely, the spatial distributions of the 6.7 GHz methanol maser spots.

Section 2 describes the criteria of target-source selection and provides details of observations and data reduction method. Section 3 presents the EAVN image, while individual sources are discussed in section 4. Section 5 focuses on the spatial morphology and feasibility of measuring the internal proper motion. Throughout this paper, sources are named from their Galactic coordinates, expressed in the form $xxx.xx+xx.xx$ following the IAU recommendation for nomenclature, unless the source has been previously named (e.g., G9.621+0.196).

2 Observations and data reduction

2.1 Source selection

The target sources were selected from the methanol maser catalog of Pestalozzi, Minier, and Booth (2005) and the methanol multibeam survey catalog (Caswell et al. 2010; Green et al. 2010) by employing the following criteria: (1) source declination $\delta > -40^\circ$, (2) catalogued peak flux density $F_p > 65$ Jy, and (3) no previous VLBI observation. These criteria were fulfilled by 34 sources. Two additional 6.7 GHz methanol maser sources, 031.28+00.06 and 049.49–00.38, were included in the target sources, despite the fact that they have been previously observed by EVN (Minier et al. 2000; Phillips & van Langevelde 2005; Surcis et al. 2012). These were used to compare the imaging capabilities of EAVN with those of EVN. The selected 36 sources, together with their properties [Galactic and IRAS names (if any), coordinates, peak velocity, peak flux density, distance, and the reference] are summarized in table 1. Most of these sources (34/36, 94%) are located in the southern hemisphere ($\delta < 0^\circ$).

2.2 EAVN array

Observations were conducted with EAVN (Shen et al. 2004), which consists of the three following VLBI networks: the Japanese VLBI Network (JVN, Doi et al. 2006), the Korean VLBI Network (KVN, Minh et al. 2003), and the Chinese VLBI Network (CVN, Ye et al. 1991). Due to the location of the EAVN stations at latitudes below 40° N, the facility is suitable for observing sources in the southern hemisphere. There are three main frequency bands of EAVN observations: 6.7, 8, and 22 GHz. The two Japanese telescopes, Yamaguchi and Hitachi, participating in this project are described in Fujisawa et al. (2002) and Yonekura et al. (2013), respectively.

Table 2. Summary of the first epoch of EAVN observations.

Session	Date (y/m/d)	Time (UT)	Telescopes*
1	2010/08/28	07:00–16:00	M, R, O, I, H, S
2	2010/08/29	07:00–28:00	M, R, O, I, H, S
3	2010/08/30	08:00–17:00	M, R, O, I, H
4	2011/10/27	03:00–10:00	M, R, O, I, Y, H
5	2011/10/28	03:00–10:00	M, R, O, I, Y, H, S
6	2011/11/26	01:30–09:00	M, R, O, I, Y, U, H, S

*M, Mizusawa; R, Iriki; O, Ogasawara; I, Ishigaki; Y, Yamaguchi; U, Usuda; H, Hitachi; S, Shanghai25.

2.3 Observations and data reduction

The first epoch observations of this monitoring project were conducted during six sessions between 2010 and 2011. Table 2 lists the observational parameters of each session, including the date, time, and participating telescopes. The locations of the telescopes are shown in figure 1. The projected baselines were from 6 M λ (Yamaguchi–Iriki) to 50 M λ (Mizusawa–Ishigaki) corresponding to fringe spacings of 34.4 mas and 4.1 mas, respectively, at 6.7 GHz. The typical size of the minor axis of the synthesized beam was 5 mas, although it varied depending on the uv-coverage.

The continuum sources, 3C454.3 and NRAO530, were used as a fringe finder and bandpass calibrator, respectively. Continuum sources located adjacent to target maser sources, J1700–2610, J1743–0350, J1845–2852, J1824+0119, and J1930+1532, were used for the delay calibration. For one source 232.62+00.99 located apart from the other sources, J0607–0834, J0609–1542, and J0730–1141 were used for the delay calibration. Five to seven maser sources were observed in each session. The integration time of a single scan of each maser source was 15 min, and scanning was repeated three or four times with an interval of 1 or 2 hr, yielding a total integration time of approximately 1 hr for each source. The data were recorded on magnetic tapes using the VSOP-terminal system at a data rate of 128 Mbps with 2-bit sampling, and correlated at the Mitaka FX correlator (Shibata et al. 1998). We selected 4 MHz including spectral lines from the recorded 32 MHz at the correlation. The selected 4 MHz bandwidths were then divided into 1024 channels, yielding a velocity coverage of 180 km s $^{-1}$ and a channel spacing of 0.178 km s $^{-1}$.

The data were reduced by using the Astronomical Image Processing System (AIPS, Greisen 2003). Correlator digitization errors were corrected by using the task ACCOR. The clock and clock-rate offsets were corrected, and the bandpass was calibrated by using the strong continuum calibrators. Next, the delay was calibrated and Doppler corrections were performed. Amplitude calibration parameters were derived from the total-power spectra of maser

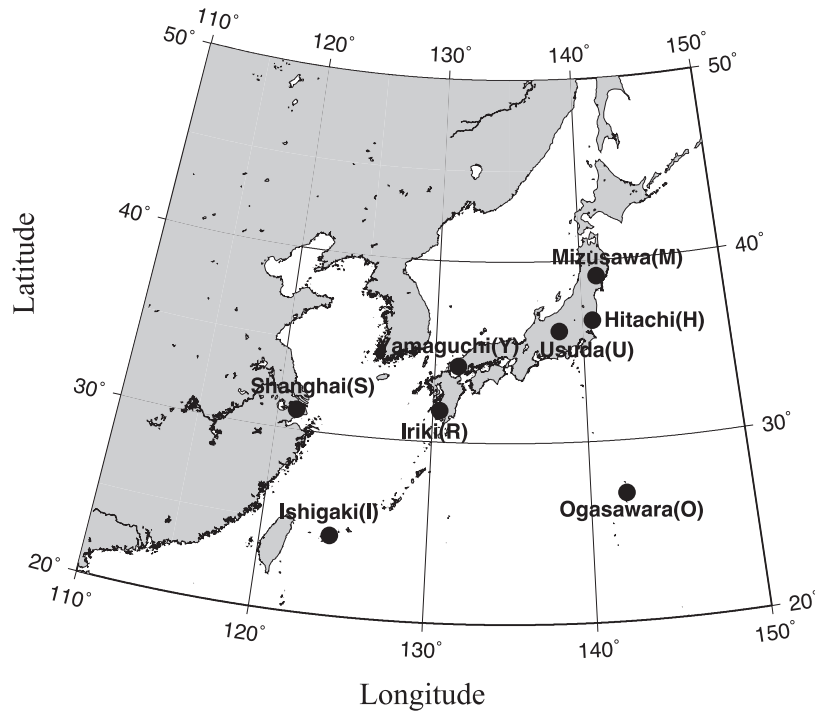


Fig. 1. Locations of the participating telescopes.

lines by using the template method in the task ACFIT. Template spectra at or near the VLBI observation date were obtained from single-dish observations of each target source with the Yamaguchi 32 m telescope. Fringe fitting was performed by using one spectral channel of the strongest maser feature, followed by self-calibration. The fringe-fitted solutions were poor for some sources at longer baselines because the maser components of these sources, including the strongest component, were heavily resolved out. At the amplitude calibration stage by using ACFIT, we flagged antennas for which calibration failed. Following calibration, uniformly weighted channel maps were made every 0.178 km s^{-1} , and maser components were searched for within the image cubes. Maser components are considered to be real if detected with signal-to-noise ratio (S/R) ≥ 5 at similar (within the beam FWHM) positions in two or more consecutive channels. Once a maser component was found, it was fitted to an elliptical Gaussian by using the task JMFIT. The identified maser spots are shown as VLBI images in the following sections.

We also used the task FRMAP for fringe-rate mapping, from which we obtained the absolute coordinates of each source with an accuracy of 200 mas. The fringe-rate map was made for selected bright maser features in each source, and the coordinates were estimated from the average of multiple solutions. The absolute coordinates estimated by fringe-rate mapping are shown in table 3. Due to

the extended north–south size of the synthesized beam for sources near the equator, nine sources suffered positional uncertainties of $\geq 1''$, and so they were excluded. The positions of the four other sources were not determined mainly due to the weak flux, and these sources are also excluded from table 3.

3 Results

The spatial distributions of the 6.7 GHz methanol maser spots were successfully obtained for all sources except 014.10+00.08, whose fringe was detected only in the Mizusawa–Hitachi baseline. Out of the 35 VLBI images, 33 were obtained for the first time. The number of reported VLBI images of 6.7 GHz methanol masers has increased by a factor of 1.5 since this study.

The VLBI images of the 35 sources, in addition to their spectra, are shown in figures 2–36. In the source spectra, the solid line and hatched box represent the total- (autocorrelation of the Hitachi 32 m data) and cross-power spectra (integrated over all baselines), respectively. The spot sizes in the VLBI images indicate the peak intensity of the spots on the logarithmic scale. Radial velocities are indicated by the color index of the color bar displayed on the right-hand side of each map. The origin of each map is the absolute source coordinates listed in table 3. The spatial scale bar is displayed at the bottom corner of each map.

Table 3. Observed parameters.*

No.	Source	Session	Coordinates (J2000.0)		V_p (km s ⁻¹)	F_p (Jy)	N_s	Scale (au ²)	V_{range} (km s ⁻¹)	Spatial morph.	F_{VLBI}/F (%)
			RA (^h ^m ^s)	Dec ([°] ['] ^{''})							
1	000.54–00.85 NW	4	17 50 14.38	–28 54 28.9	8.7	0.5	3	9 × 3	[8.5, 8.9]	C	14
	000.54–00.85 SE		17 50 14.56	–28 54 31.4	13.3	63.2	55	3900 × 4500	[10.8, 19.6]	E	35
2	000.64–00.04	5	17 47 18.69	–28 24 25.3	49.6	6.1	17	1300 × 760	[48.2, 52.4]	C	11
3	002.53+00.19 [‡]	3			3.4	7.8	34	750 × 2100	[3.0, 19.0]	E	12
4	006.18–00.35	2	18 01 02.17	–23 47 10.8	–30.2	7.5	18	1400 × 1100	[–36.3, –29.6]	C	4
5	006.79–00.25	2	18 01 57.76	–23 12 34.2	26.1	24.2	72	1400 × 640	[15.0, 30.8]	E	36
6	008.68–00.36	1	18 06 23.48	–21 37 10.4	43.1	21.1	25	970 × 590	[40.7, 44.4]	C	9
7	008.83–00.02	1	18 05 25.66	–21 19 25.4	–3.7	16.7	29	1400 × 990	[–5.7, 2.6]	E	7
8	009.61+00.19	6	18 06 14.91	–20 31 43.4	5.5	8.3	31	490 × 120	[4.9, 6.9]	L	22
9	009.98–00.02	6	18 07 50.12	–20 18 56.5	42.4	18.9	58	3000 × 1600	[40.7, 50.7]	C	32
10	010.32–00.16	4	18 09 01.47	–20 05 07.8	11.6	21.1	22	490 × 620	[4.1, 14.2]	C	19
11	011.49–01.48	4	18 16 22.13	–19 41 27.2	6.3	28.8	68	290 × 710	[4.5, 17.1]	C	42
12	011.90–00.14	4	18 12 11.45	–18 41 28.8	43.1	38.3	29	1300 × 480	[39.6, 44.2]	P	41
13	012.02–00.03	3	18 12 01.86	–18 31 55.9	108.3	22.8	25	520 × 1200	[107.1, 109.0]	A	18
14	012.68–00.18 [‡]	3			58.4	11.5	20	310 × 650	[52.0, 60.1]	C	1
15	012.88+00.48	5	18 11 51.39	–17 31 30.1	39.2	18.0	67	2600 × 3800	[29.9, 40.1]	C	21
16	014.10+00.08 [‡]	5									
17	020.23+00.06 SW	5	18 27 44.56	–11 14 54.1	71.5	3.2	12	160 × 280	[71.1, 73.6]	P	14
	020.23+00.06 NE		18 27 44.95	–11 14 47.8	60.9	1.1	14	100 × 10	[60.2, 71.1]	A	24
18	023.43–00.18 MM1	1	18 34 39.19	–08 31 25.3	96.6	5.0	10	110 × 110	[96.3, 98.4]	C	7
	023.43–00.18 MM2		18 34 39.27	–08 31 39.3	103.0	8.1	28	1600 × 550	[101.4, 107.9]	P	6
19	025.65+01.05 [†]	1			41.8	26.3	8	90 × 20	[41.5, 42.2]	L	15
20	025.71+00.04	1	18 38 03.15	–06 24 15.0	95.5	34.1	13	930 × 1500	[89.8, 96.2]	C	4
21	025.82–00.17	6	18 39 03.63	–06 24 09.9	91.6	8.2	53	1500 × 1500	[90.5, 99.5]	E	29
22	028.83–00.25 [†]	2			83.5	18.4	30	1700 × 2000	[81.2, 92.1]	A	15
23	029.86–00.04 [†]	6			101.7	22.1	53	1400 × 3200	[99.5, 105.1]	A	56
24	030.70–00.06 [†]	2			88.3	71.7	14	4100 × 2500	[85.7, 89.4]	P	28
25	030.76–00.05 [†]	5			91.7	10.6	15	160 × 20	[90.5, 92.6]	P	29
26	030.91+00.14 [†]	2			101.9	3.5	10	150 × 320	[100.1, 103.0]	L	2
27	031.28+00.06 [†]	4			110.5	8.2	38	3300 × 2700	[104.3, 112.4]	C	11
28	032.03+00.06 [†]	3			92.7	27.8	28	2100 × 3100	[92.1, 101.4]	P	25
29	037.40+01.52 [†]	3			41.1	24.0	4	60 × 20	[41.0, 41.5]	L	4
30	049.49–00.38	3	19 23 43.93	+14 30 35.1	59.3	134.9	21	2000 × 1700	[51.7, 60.2]	C	13
31	232.62+00.99	2	07 32 09.78	–16 58 12.4	22.9	64.4	11	40 × 120	[21.9, 23.4]	P	29
32	351.77–00.53	1	17 26 42.54	–36 09 17.6	1.7	4.4	18	40 × 40	[–2.7, 2.1]	E	1
33	352.63–01.06	1	17 31 13.93	–35 44 08.5	–2.9	140.4	32	330 × 260	[–5.6, –2.0]	L	58
34	353.41–00.36	2	17 30 26.18	–34 41 45.6	–20.5	72.7	16	220 × 460	[–21.5, –19.6]	C	48
35	354.61+00.47	2	17 30 17.09	–33 13 55.0	–24.4	26.5	63	1500 × 1700	[–25.8, –15.6]	C	9
36	359.43–00.10 [‡]	3			–46.8	11.2	5	1200 × 370	[–52.4, –46.6]	P	6

*Column 1: ID number (as listed in table 1), column 2: Source name, column 3: Observational session (corresponding to the sessions listed in table 2), columns 4 and 5: Absolute coordinates obtained by fringe-rate mapping, columns 6 and 7: Radial velocity and flux density of the peak maser spot located at the origin of each map respectively, column 8: Number of detected maser spots, columns 9 and 10: Spatial scale (in RA and Dec) and velocity range of the detected component respectively, column 11: Spatial morphology (E, Elliptical; A, Arched; L, Linear; P, Paired; C, Complex), column 12: Ratio of integrated fluxes of cross- to total-power spectra.

[†]Sources not suitable for fringe-rate mapping because of the equatorial location.

[‡]Sources not suitable for fringe-rate mapping because of weak flux or resolved-out.

Besides the coordinates, table 3 lists the following observational parameters: the radial velocity and flux density of the peak maser spot, number of detected maser spots, spatial scale (in right ascension and declination), velocity range of the detected spectrum, morphological

type, and ratio of integrated fluxes of cross- to the total-power spectrum of each source. As mentioned in the following subsection, we consider that three sources contain two separated star-forming regions in each image, yielding 38 imaged sources. The numbers of detected spots in

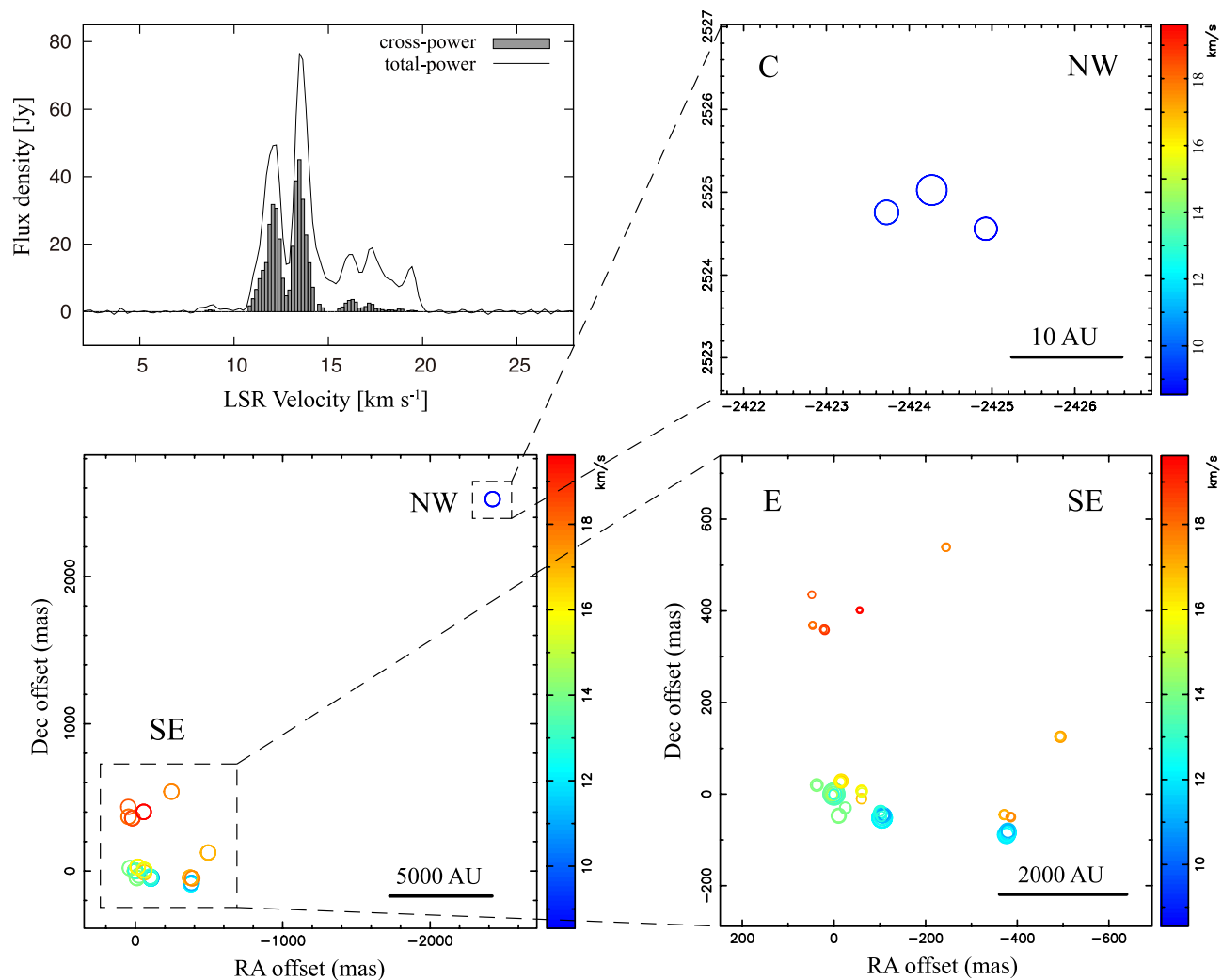


Fig. 2. The 6.7 GHz methanol maser emissions of source 000.54–00.85. Left-hand upper panel: Total-power (solid line) and cross-power (hatched box) spectra. Left-hand lower and right-hand panels: Spatial distributions of the methanol maser spots obtained from the EAVN observations and the morphological type in the left-hand upper corner. Details are provided in section 4.

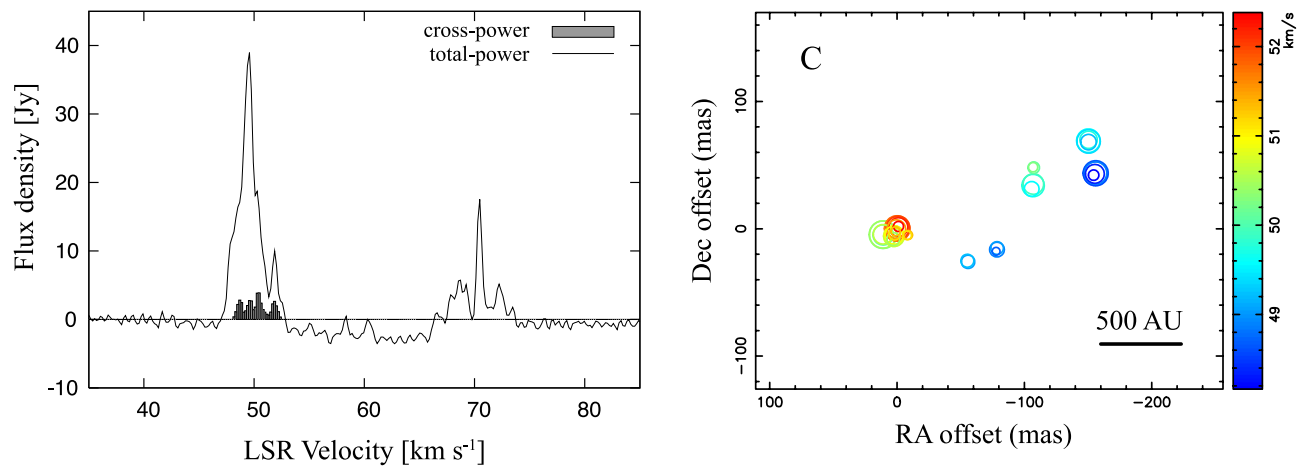


Fig. 3. Data for source 000.64–00.04, plotted the same as in figure 2.

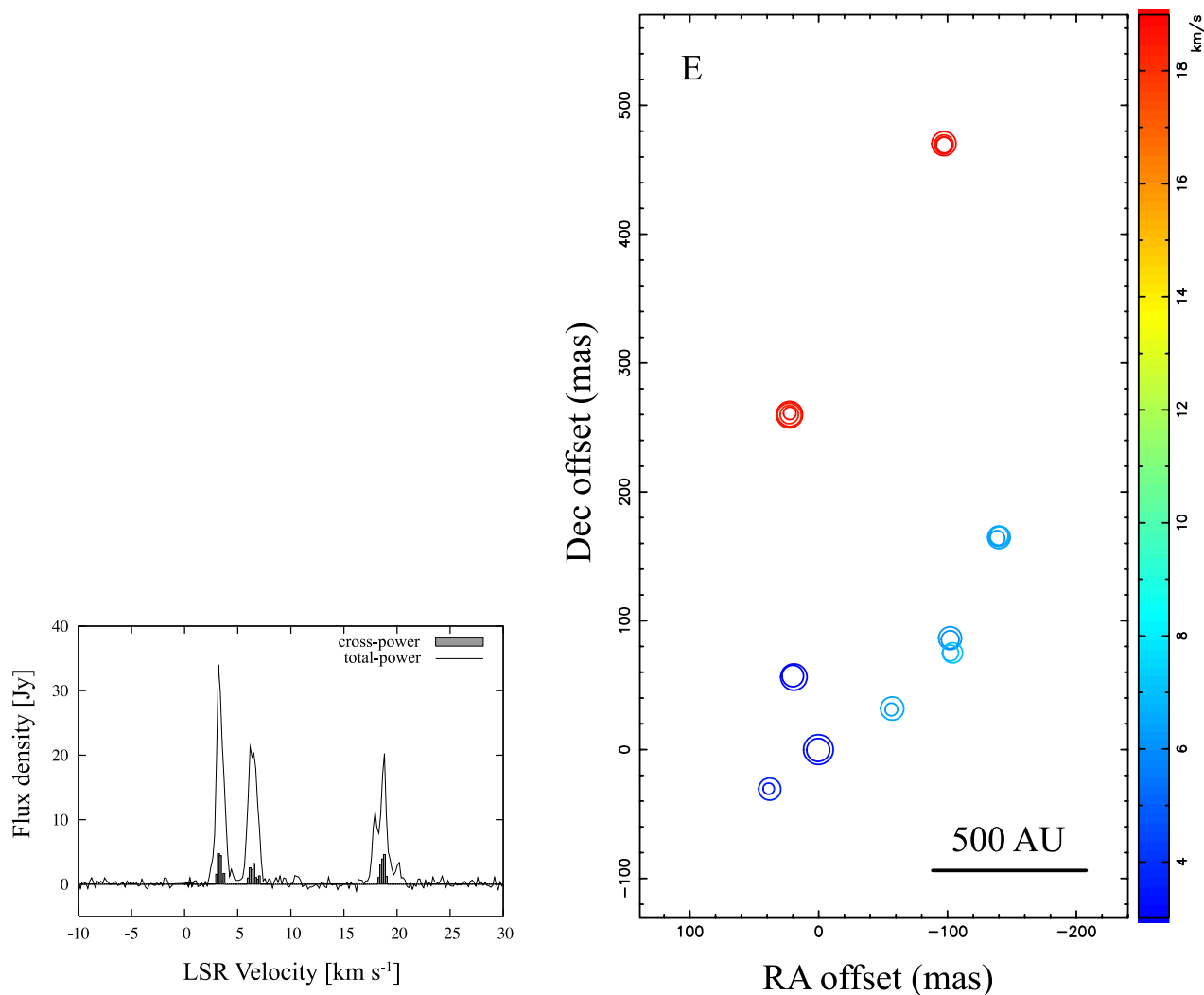


Fig. 4. Data for source 002.53+00.19, plotted the same as in figure 2.

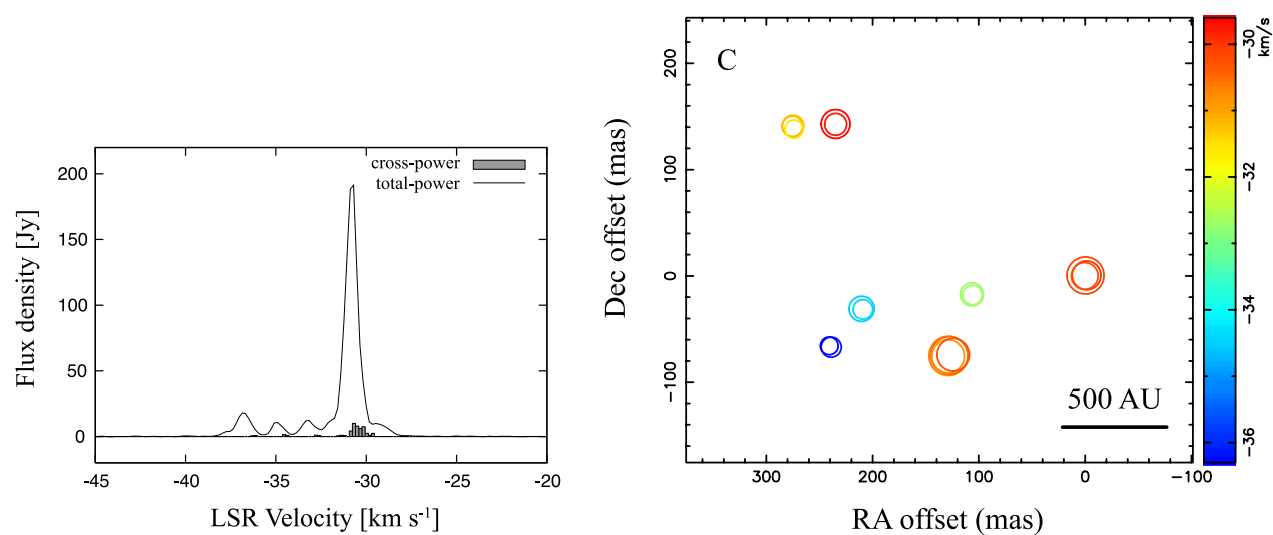


Fig. 5. Data for source 006.18-00.35, plotted the same as in figure 2.

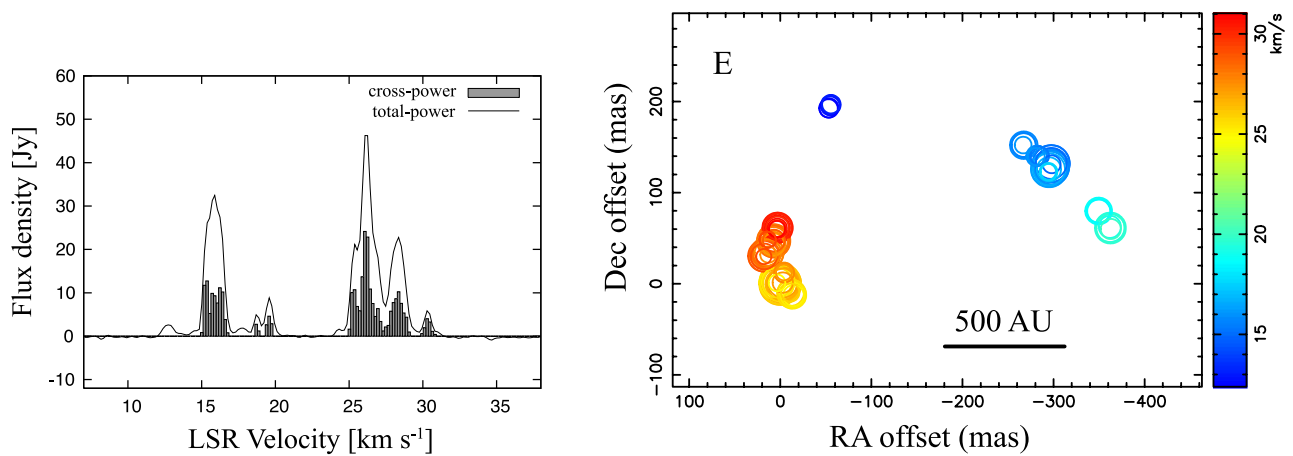


Fig. 6. Data for source 006.79–00.25, plotted the same as in figure 2.

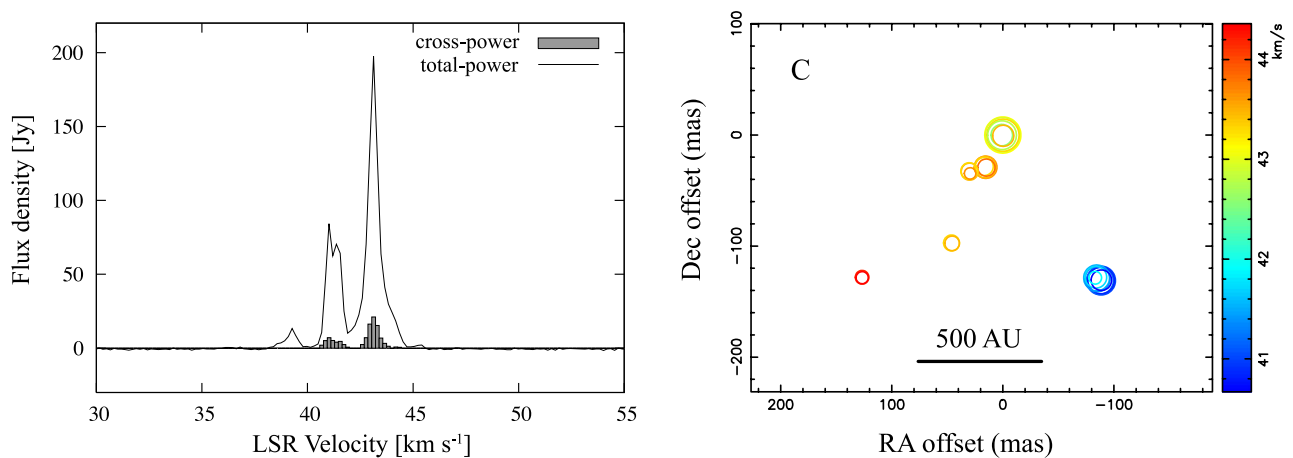


Fig. 7. Data for source 008.68–00.36, plotted the same as in figure 2.

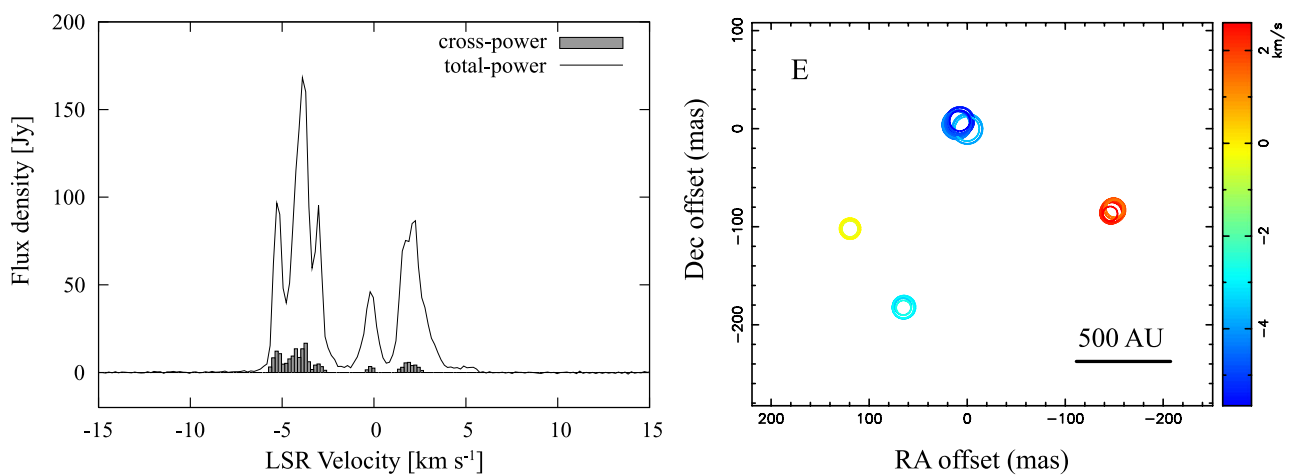


Fig. 8. Data for source 008.83–00.02, plotted the same as in figure 2.

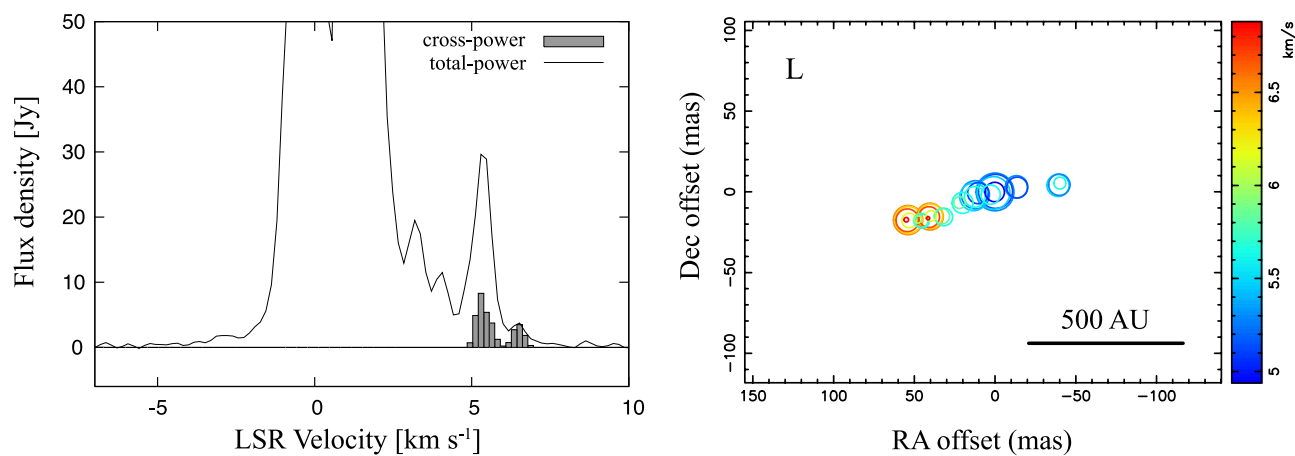


Fig. 9. Data for source 009.61+00.19, plotted the same as in figure 2.

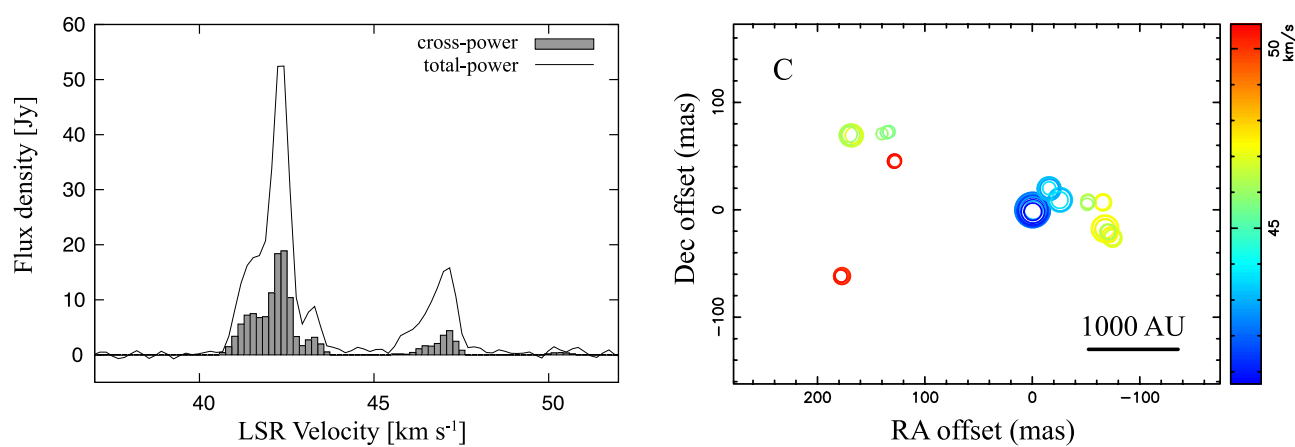


Fig. 10. Data for source 009.98-00.02, plotted the same as in figure 2.

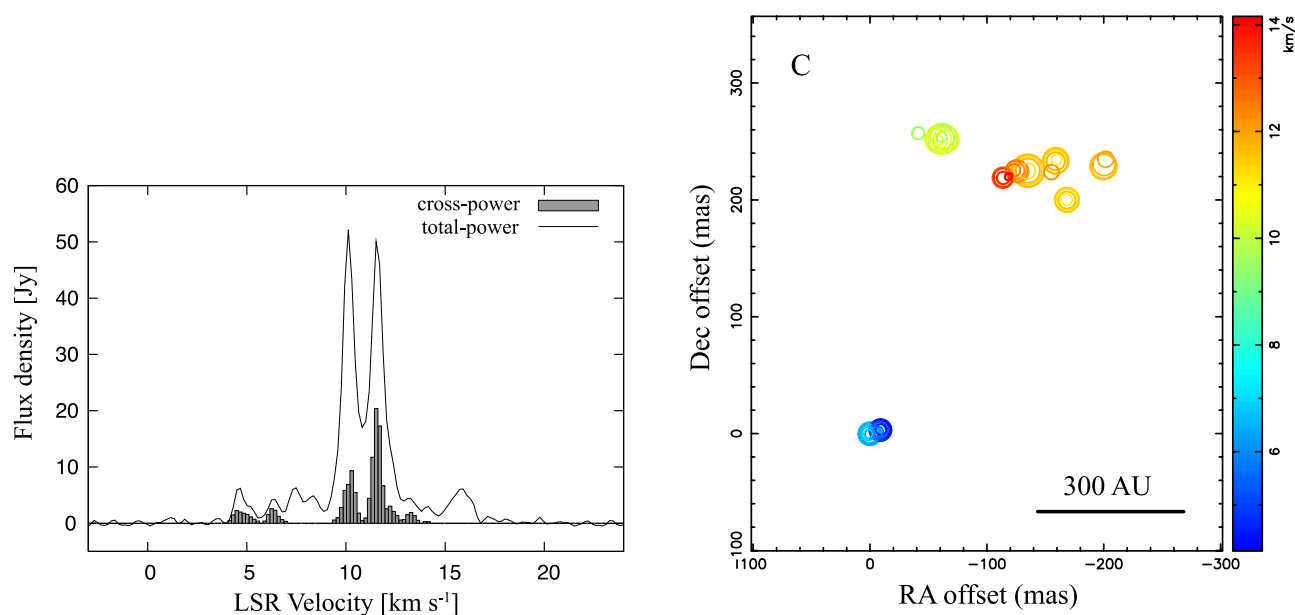


Fig. 11. Data for source 010.32-00.16, plotted the same as in figure 2.

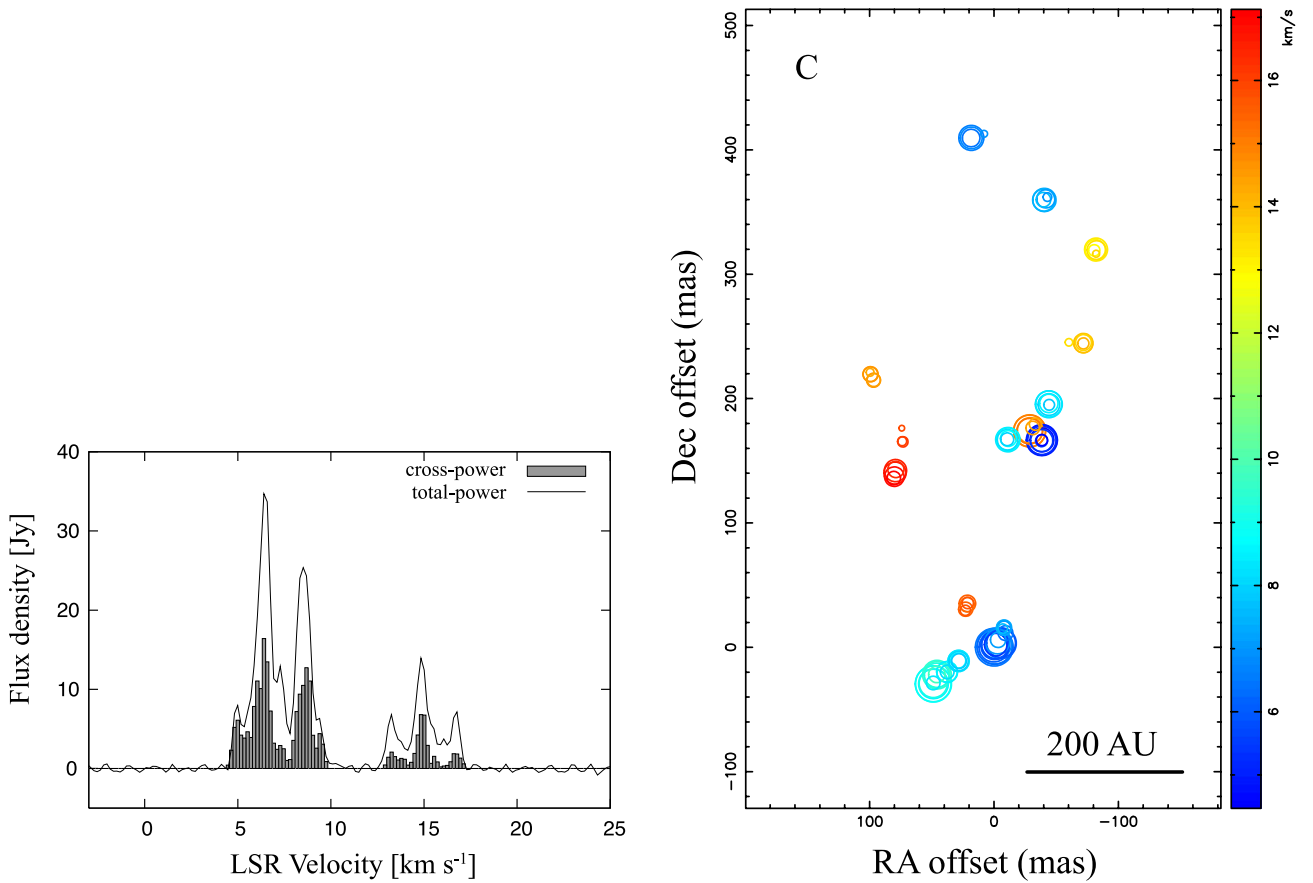


Fig. 12. Data for source 011.49–01.48, plotted the same as in figure 2.

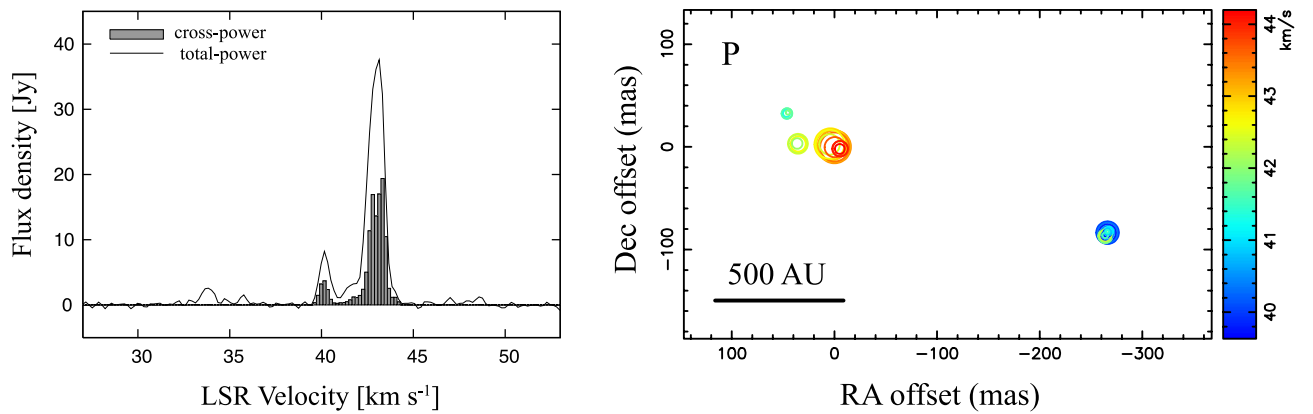


Fig. 13. Data for source 011.90–00.14, plotted the same as in figure 2.

individual sources vary from 3 to 72, with 34 sources (89%) displaying at least 10 spots. The spatial scale of the maser distribution is from 9 to 4900 astronomical units (au).

Following Bartkiewicz et al. (2009), we have classified the observed morphology into the five following types: Elliptical, Arched, Linear, Paired, and Complex, as shown in table 3. Since the classification was made by eye, it is not strict, but provides an indication of the morphological

structure. In the classification process, we used only the spatial distribution of the spots; the velocity distribution was not considered. The classification process is as follows: First, we recognized that almost all spots form small clusters, where we define a cluster here as a spot group including one or more spots, and the size is roughly one tenth of the total extent. When only two clusters exist in a source, the source is classified as *Paired*. When three or more clusters exist and all of them are successively and

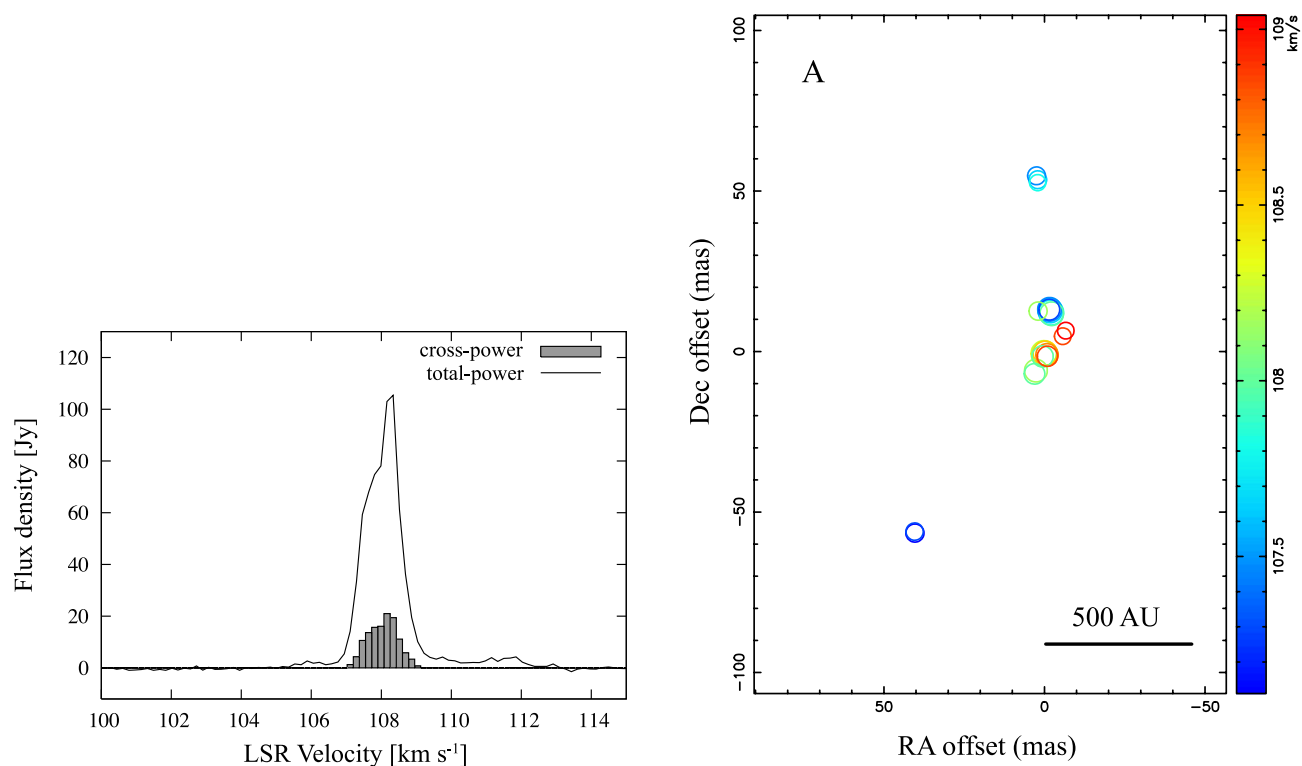


Fig. 14. Data for source 012.02–00.03, plotted the same as in figure 2.

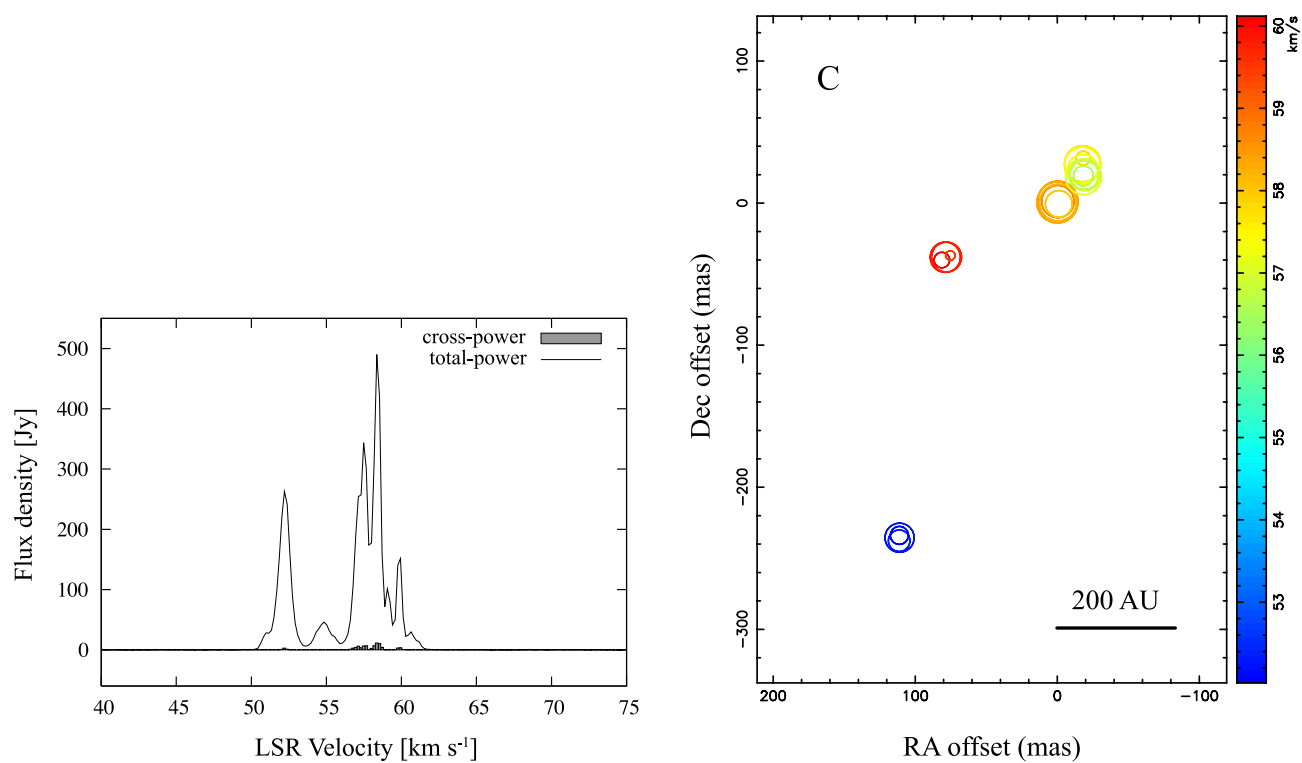


Fig. 15. Data for source 012.68–00.18, plotted the same as in figure 2.

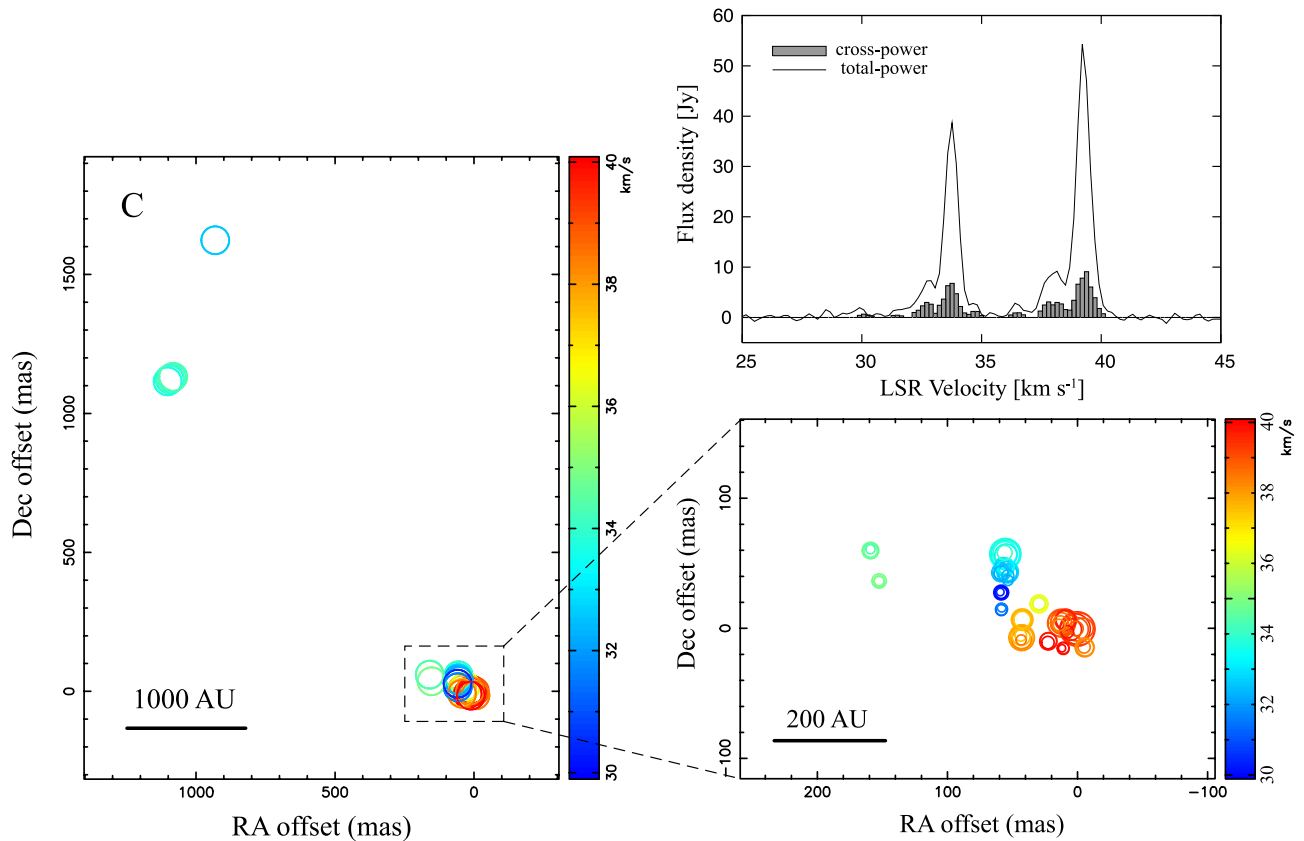


Fig. 16. Data for source 012.88+00.48, plotted the same as in figure 2.

linearly distributed, the source is *Linear*. When three or more clusters exist and all are distributed successively, but loosely curved ($<45^\circ$), the source is *Arched*. When four or more clusters exist and all are applicable to an ellipse, the source is *Elliptical*. The remaining sources are classified as *Complex*.

4 Comments on individual sources

000.54–00.85. The main cluster (SE) of the 6.7 GHz methanol maser spots of this source are distributed over $540 \text{ mas} \times 630 \text{ mas}$, corresponding to $3900 \text{ au} \times 4500 \text{ au}$, at a near kinematic distance of 7.2 kpc (figure 2). This source has the largest extension, at 4900 au, of all imaged sources. The distance is determined from the radial velocity and the H I self-absorption (H I SA) spectrum. Isolated spots (NW) located at $3''$ ($2 \times 10^4 \text{ au}$) north-west are probably associated with another excitation source. The distribution of the maser spots of the main cluster is *Elliptical*, having roughly circular morphology, while that of NW component is *Complex*. These maser spots correspond to spots labeled A–L in the Australia Telescope Compact Array (ATCA) image (IRAS 17470–2853, Walsh et al. 1998), while the

isolated spots in the EAVN image correspond to spot M in the ATCA image.

000.64–00.04. This source is associated with a famous high-mass star-forming region in the Galactic center Sgr B2 located at a trigonometric parallax distance of 7.9 kpc (Reid et al. 2009). The wide absorption trough in the spectrum is remarkable (Menten 1991). The methanol maser spots in this source show *Complex* spatial distribution over $170 \text{ mas} \times 100 \text{ mas}$, corresponding to $1300 \text{ au} \times 760 \text{ au}$ at the source (figure 3). These maser spots are extended roughly along the east–west direction, although the extension is not clearly linear. The ATCA image (IRAS 17441–2822, Walsh et al. 1998) extends along the north–east–south–west direction. Apart from the contradicting elongation direction, the EAVN and ATCA images display similar radial velocity gradient trends, from red-shifted at the east to blue-shifted at the west.

002.53+00.19. The kinematic distance of this source is 4.2 kpc. Although the north-western part is missing, the spatial distribution is *Elliptical* (figure 4). The maser spots are distributed over $180 \text{ mas} \times 500 \text{ mas}$, corresponding to a linear area of $750 \text{ au} \times 2100 \text{ au}$. The millimeter and sub-millimeter emissions have been previously detected at this maser position (Hill et al. 2005; Walsh et al. 2003).

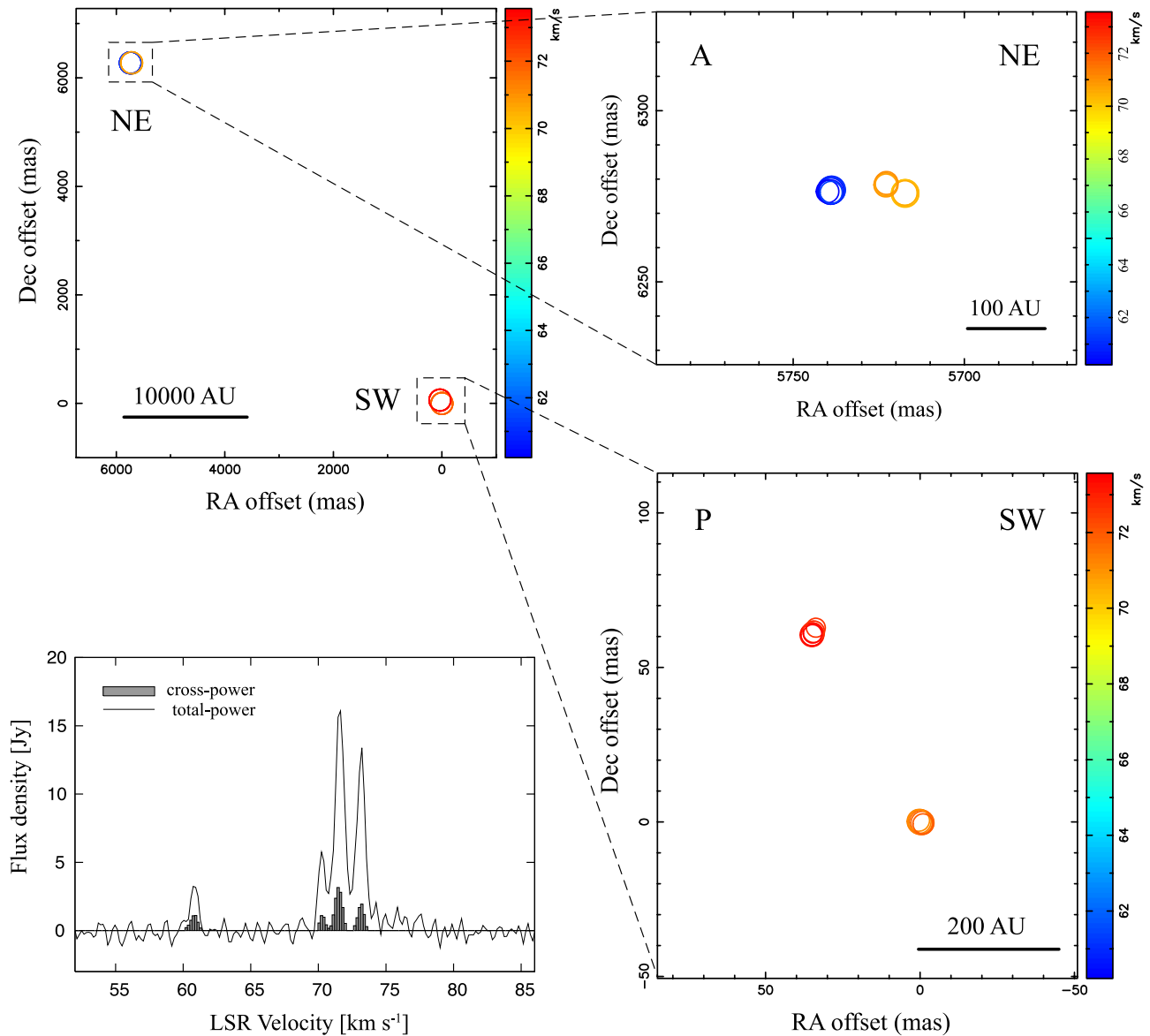


Fig. 17. Data for source 020.23+00.06, plotted the same as in figure 2.

006.18–00.35. This source is located at the same line of sight toward the W 28 supernova remnant field. The 6.7 GHz methanol maser source seems to be associated with one of several dense molecular cores previously identified in this region, namely, Core 3 (Nicholas et al. 2011). The radial velocity (-33 km s^{-1}) of Core 3 approximates that of the spectral peak of the methanol maser but differs largely from those of other molecular cores. Dame and Thaddeus (2008) suggested that this source is located in the galactic 3 kpc arm approximately 5 kpc from the Sun. Therefore, Core 3 (and hence the methanol maser source) is likely not connected to the gas associated with the W 28 field (Nicholas et al. 2011). We assumed a source distance of 5.1 kpc (Green & McClure-Griffiths 2011). The morphology is *Complex* (figure 5). The maser spots

are distributed over $280 \text{ mas} \times 220 \text{ mas}$, corresponding to $1400 \text{ au} \times 1100 \text{ au}$.

006.79–00.25. This source also is located near the supernova remnant W 28, similarly in the case 006.18–00.35, and appears to be associated with Core 1, as defined by Nicholas et al. (2011). The radial velocity of $+21 \text{ km s}^{-1}$ of the ammonia line of Core 1 indicates a kinematic distance of 3.8 kpc, although the uncertainty is large. The spatial distribution of the masers is clearly *Elliptical*, with a clockwise radial velocity gradient (figure 6). The size of this ellipse is 400 mas from east to west, corresponding to 1400 au.

008.68–00.36. This source is located at a distance of 4.5 kpc (Green & McClure-Griffiths 2011). The spatial distribution of the masers is *Complex* (figure 7). The maser spots are distributed over $220 \text{ mas} \times 130 \text{ mas}$,

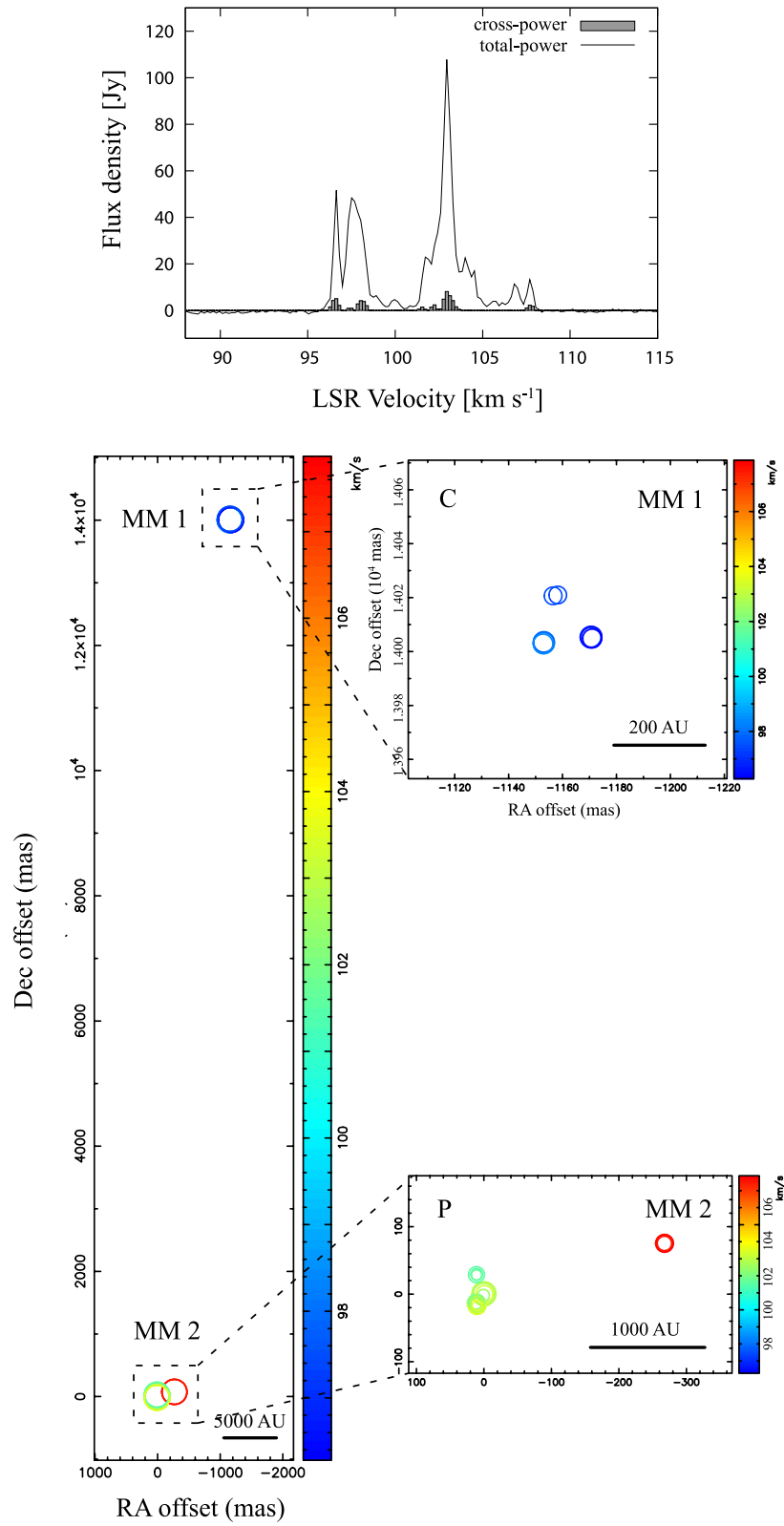


Fig. 18. Data for source 023.43–00.18, plotted the same as in figure 2.

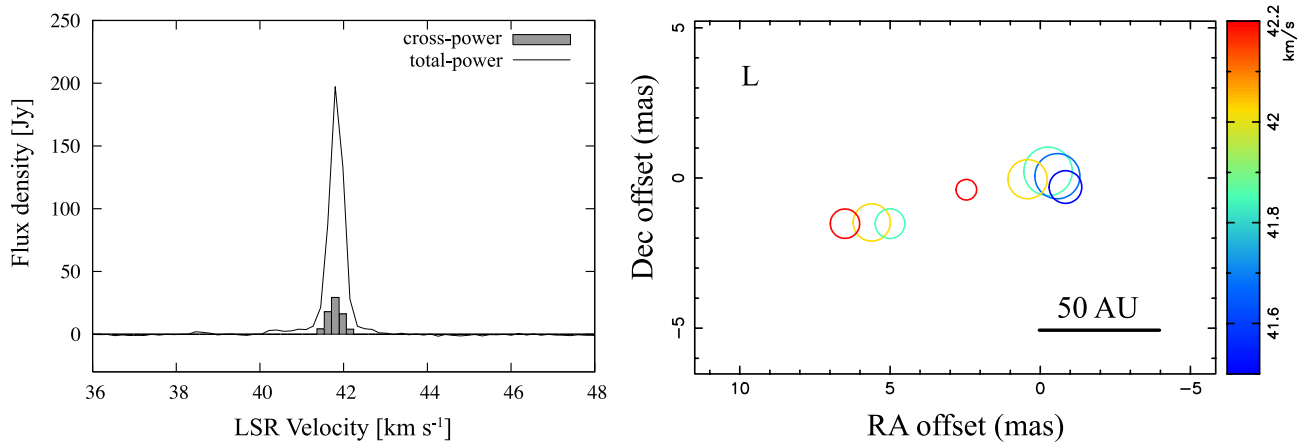


Fig. 19. Data for source 025.65+01.05, plotted the same as in figure 2.

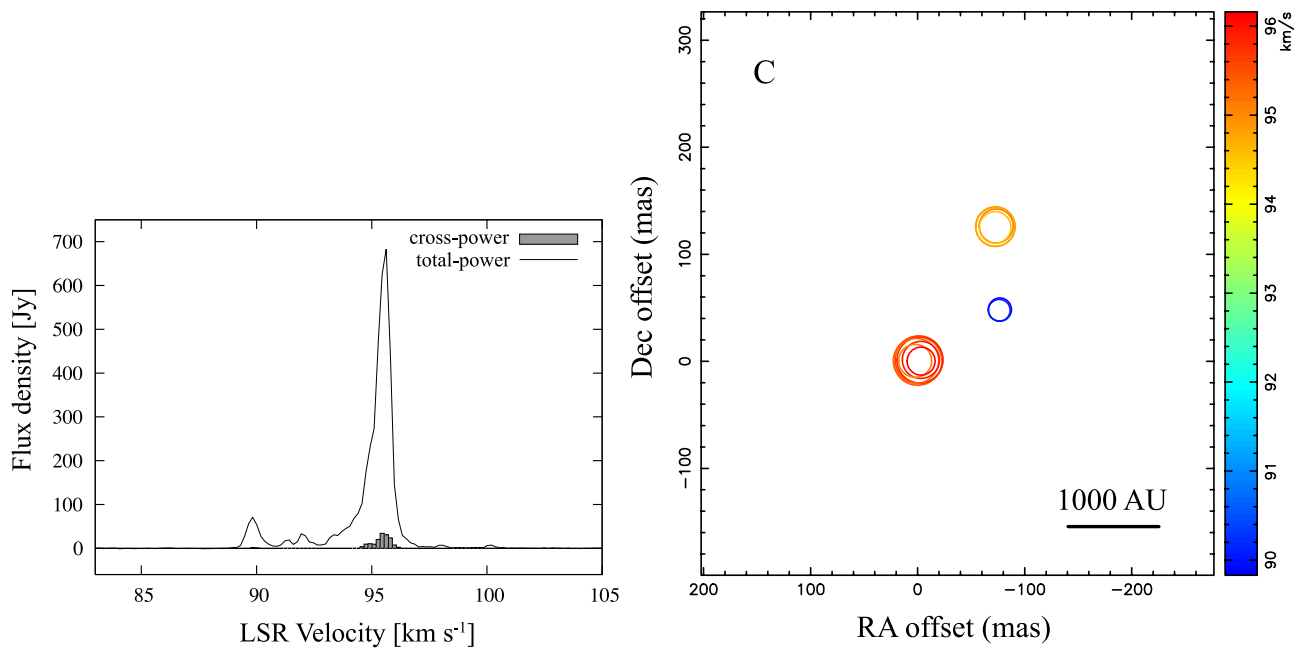


Fig. 20. Data for source 025.71+00.04, plotted the same as in figure 2.

corresponding to $970 \text{ au} \times 590 \text{ au}$. These maser spots coincide well with those labeled A–D in the ATCA image (IRAS 18032–2137, Walsh et al. 1998). The 6.7 GHz methanol masers are located at the center of the continuum emission and the foot-point of the ^{12}CO ($J = 2-1$) outflow [where the ^{12}CO ($J = 2-1$) and 1.2 mm continuum images were obtained by the SMA (Longmore et al. 2011)]. The ^{12}CO (1–0) and ^{12}CO (2–1) line profiles show prominent infall signatures (Ren et al. 2012). The methanol maser is associated with the weaker of two submillimeter continuum cores known to exist in this region (Walsh et al. 2003). 008.83–00.02. This source is located at a distance of 5.2 kpc (Green & McClure-Griffiths 2011). The morphology is *Elliptical* but displays no simple velocity

gradient (figure 8). The maser spots are distributed over $270 \text{ mas} \times 190 \text{ mas}$, corresponding to $1400 \text{ au} \times 990 \text{ au}$. 009.61+00.19. Trigonometric parallax measurements established the distance of this source as 5.2 kpc (Sanna et al. 2009). Various H II regions at different evolutionary phases exist in this region, labeled A–E by Garay et al. (1993). Source 009.61+00.19 is associated with D, the ultracompact H II region. The other component, E, located $10''$ north of D, is a candidate hypercompact H II region (Kurtz & Franco 2002), which is well known as the strongest 6.7 GHz methanol maser, G9.621+0.196. Within this complex region, we imaged only 009.61+00.19, although the strongest emission in the peak total-power spectrum arises from G9.621+0.196. The

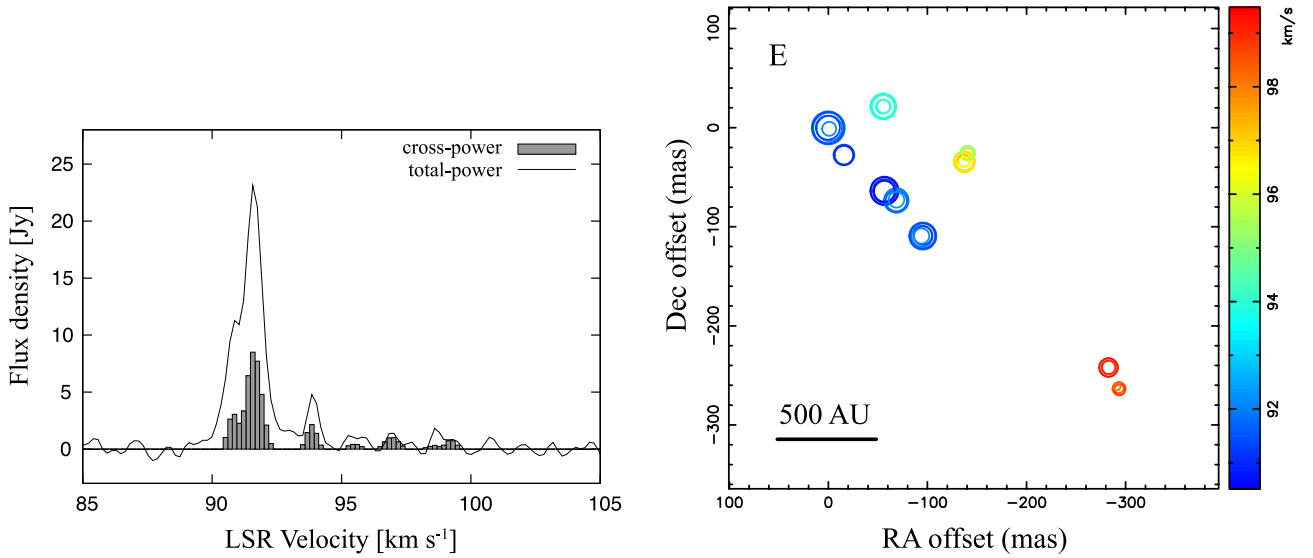


Fig. 21. Data for source 025.82–00.17, plotted the same as in figure 2.

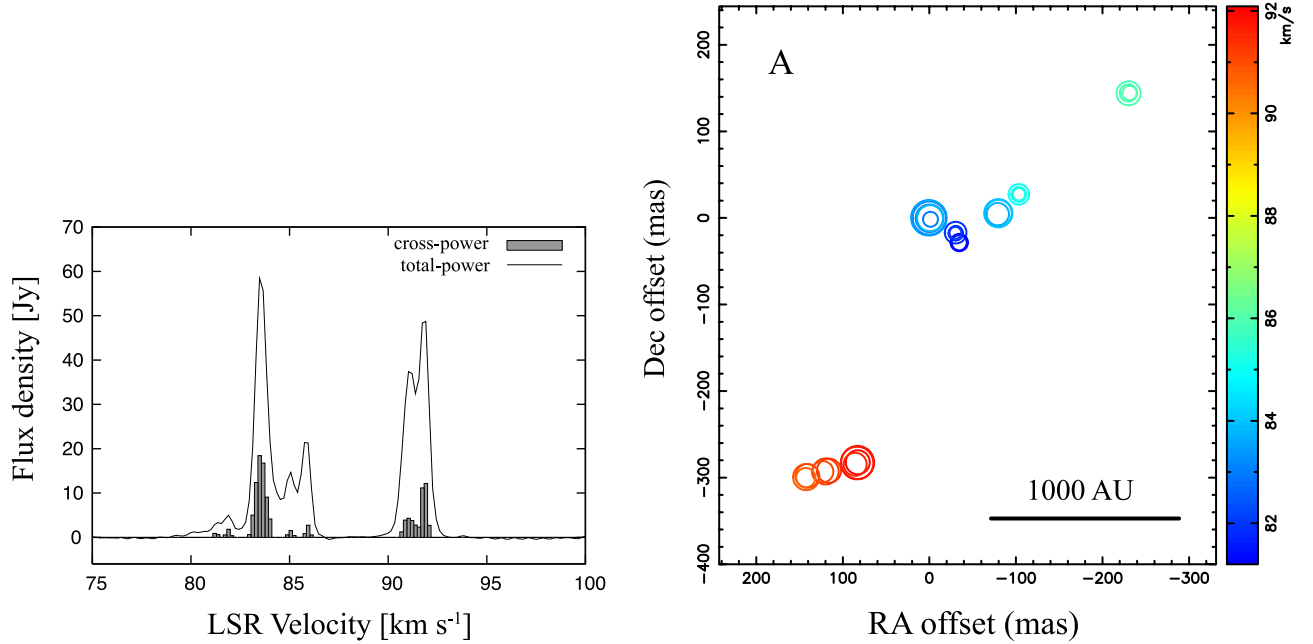


Fig. 22. Data for source 028.83–00.25, plotted the same as in figure 2.

EAVN image reveals a *Linear* distribution of the methanol maser spots, orienting in the east–west direction with a linear velocity gradient (figure 9). The spots are distributed over $100 \text{ mas} \times 20 \text{ mas}$, corresponding to $490 \text{ au} \times 120 \text{ au}$ at the source. Only two spots appear in the ATCA image (IRAS 18032–2032, Walsh et al. 1998; Phillips et al. 1998). 009.98–00.02. This source is located at a distance of 12.0 kpc (Green & McClure-Griffiths 2011). The 6.7 GHz methanol maser spots show a *Complex* spatial distribution with no obvious trend in the velocity distribution (figure 10). The scale coverage is $250 \text{ mas} \times 130 \text{ mas}$,

corresponding to $3000 \text{ au} \times 1600 \text{ au}$ at the source. The maser spots correspond to those labeled A–F in the ATCA image (IRAS 18048–2019, Walsh et al. 1998). We detected new maser spots at $V_{\text{lsr}} = 49.98\text{--}50.68 \text{ km s}^{-1}$, located at $(\Delta\alpha, \Delta\delta) = (+130, +45)$ and $(+180, -60)$ mas from the brightest spot at the origin of the image. The flux density of these new spots is 1.5 Jy, which is similar to that observed in the single-dish spectrum obtained by Parkes 64 m (Green et al. 2010).

010.32–00.16. The distance of this source is assumed to be 2.39 kpc, a measured distance of W 31 North (Moisés et al.

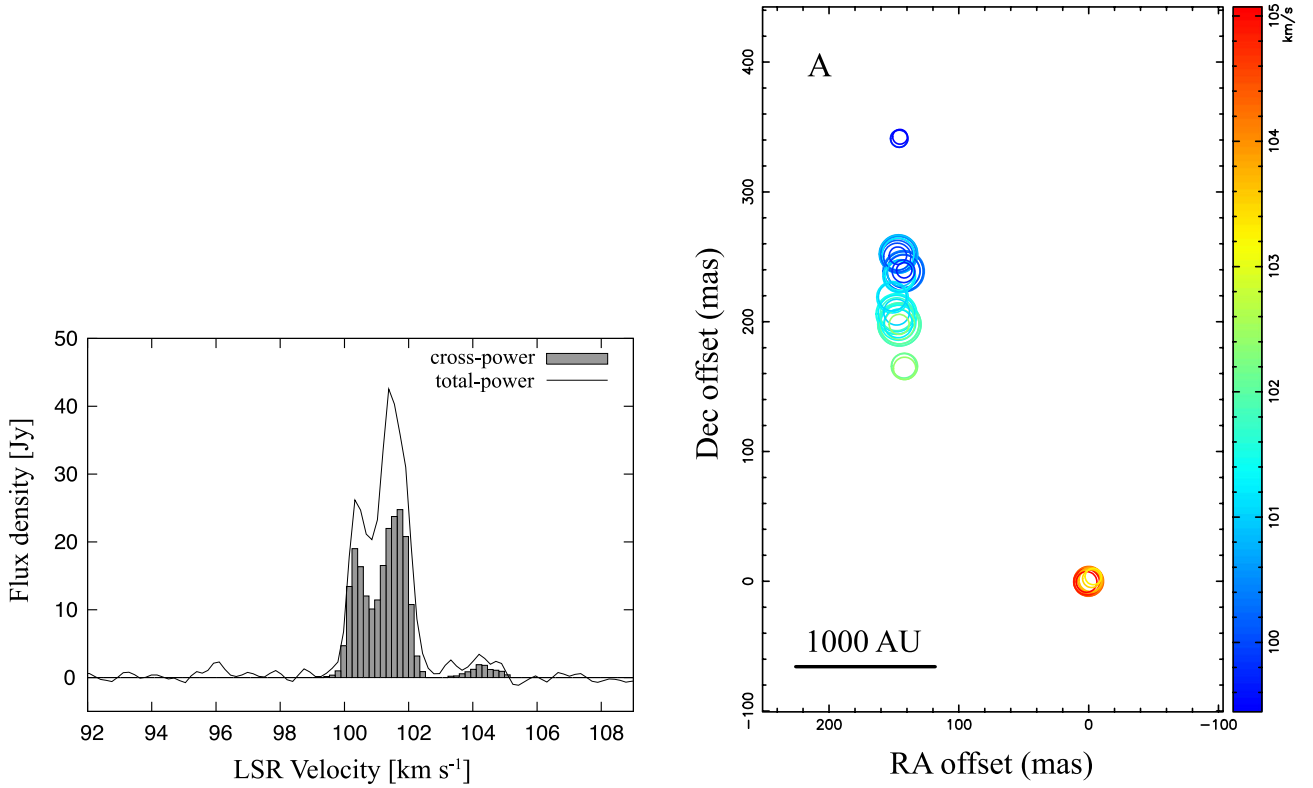


Fig. 23. Data for source 029.86–00.04, plotted the same as in figure 2.

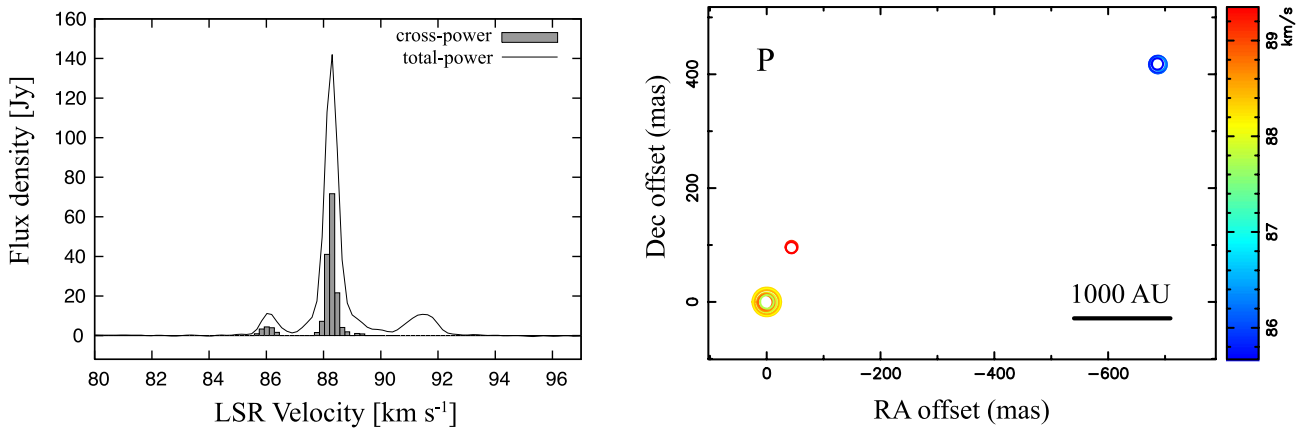


Fig. 24. Data for source 030.70–00.06, plotted the same as in figure 2.

2011), with which it is associated. It should be noted that there is a dispute about this source distance in the literature (Green & McClure-Griffiths 2011 and references therein). The 6.7 GHz methanol maser spots show *Complex* spatial distribution over 200 mas \times 260 mas, corresponding to 490 au \times 620 au at the source (figure 11). The maser spots clustering in the northern part of the image correspond to those labeled E–H in the ATCA image (IRAS 18060–2005, Walsh et al. 1998). We detected new maser spots at $V_{\text{lsr}} = 4.14\text{--}6.95 \text{ km s}^{-1}$, located 220 mas south from the main cluster. The origin of the image does not coincide

with the position of the strongest component, but a relatively strong, compact component at $V_{\text{lsr}} = 6.3 \text{ km s}^{-1}$ is selected for the origin of the image.

011.49–01.48. This source displays *Complex* spatial and velocity distributions of its methanol masers (figure 12). The overall distribution is elongated along the north–south direction over 180 mas \times 440 mas, corresponding to 290 au \times 710 au at a kinematic distance of 1.6 kpc. These maser spots coincide with those labeled A–M in the ATCA image (IRAS 18134–1942, Walsh et al. 1998). New maser spots at $V_{\text{lsr}} = 6.40\text{--}6.76$ and $6.93\text{--}7.63 \text{ km s}^{-1}$ are detected

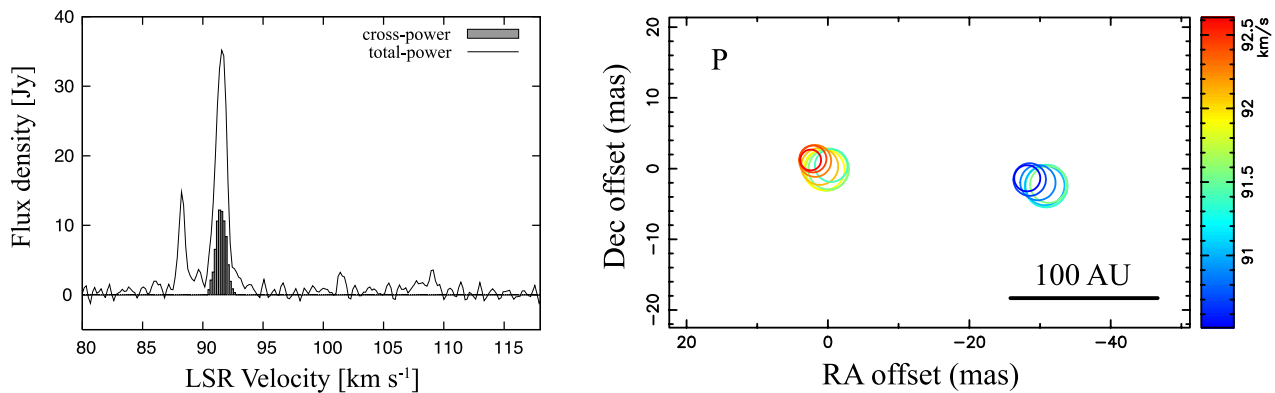


Fig. 25. Data for source 030.76+00.05, plotted the same as in figure 2.

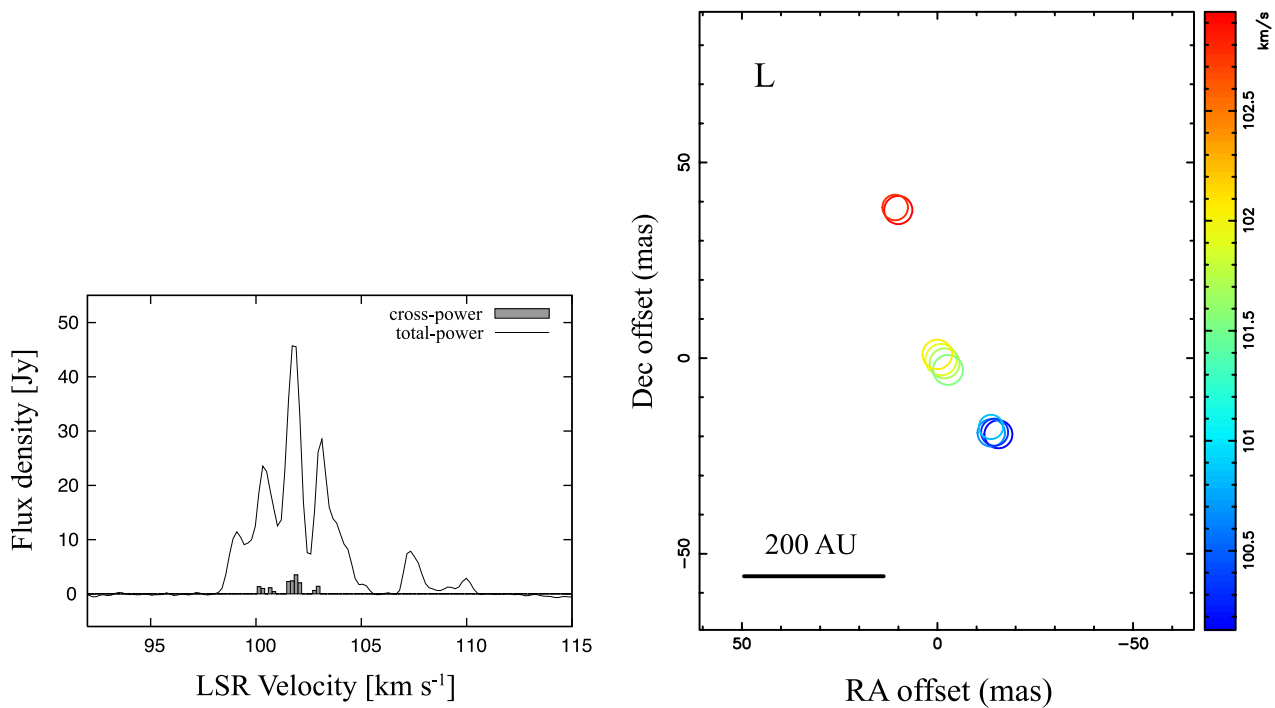


Fig. 26. Data for source 030.91+00.14, plotted the same as in figure 2.

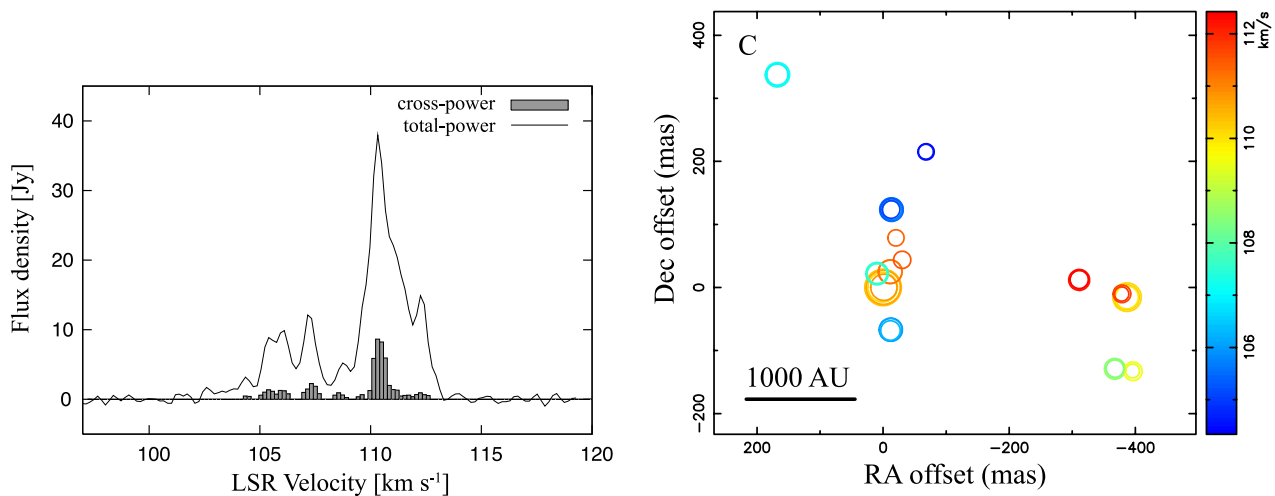


Fig. 27. Data for source 031.28+00.06, plotted the same as in figure 2.

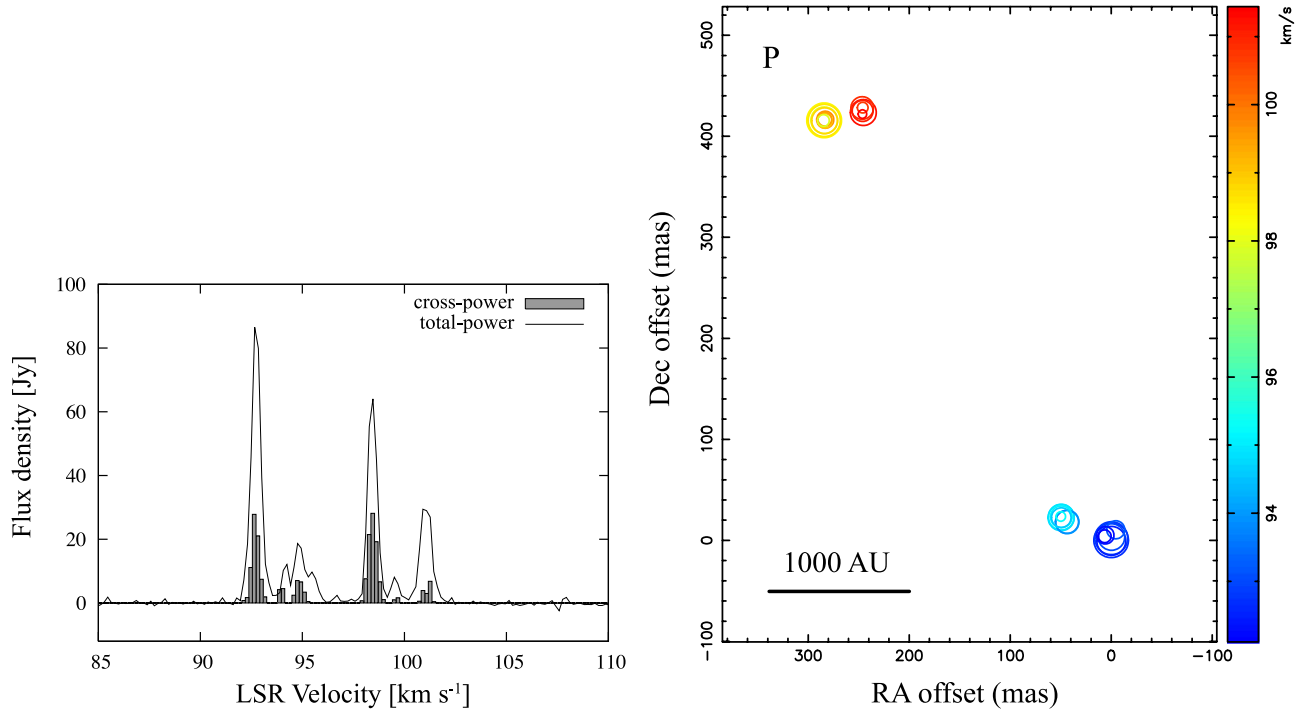


Fig. 28. Data for source 032.03+00.06, plotted the same as in figure 2.

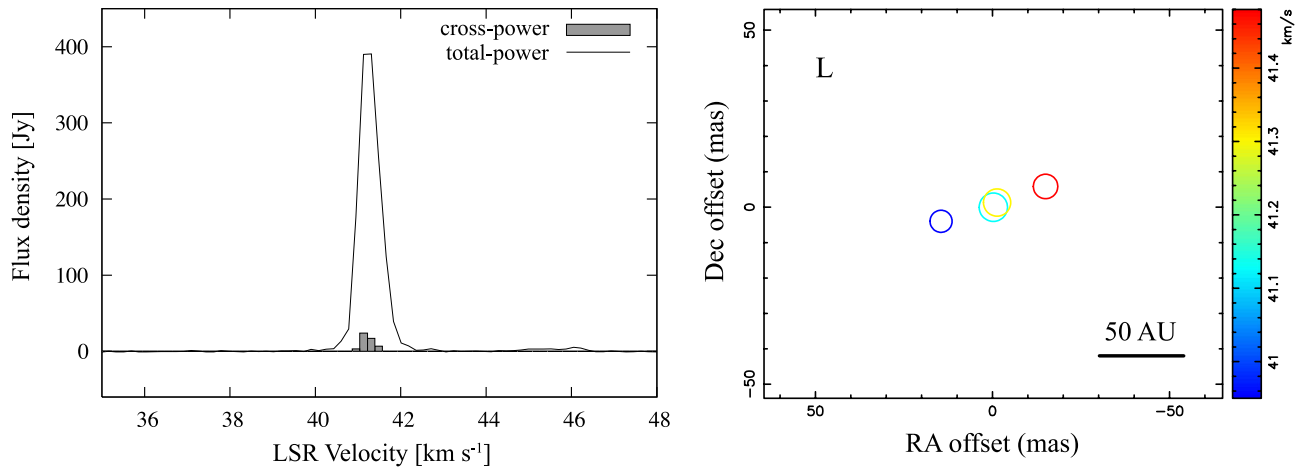


Fig. 29. Data for source 037.40+01.52, plotted the same as in figure 2.

at $(\Delta\alpha, \Delta\delta) = (+18, +409)$ and $(-40, +360)$ mas from the brightest spot, respectively.

011.90–00.14. The observed maser spots of this source display a *Paired* distribution (figure 13), divided into two spatially discrete clusters separated by 340 mas, corresponding to 1300 au at a near kinematic distance of 4.0 kpc (Green & McClure-Griffiths 2011).

012.02–00.03. This source is located at a distance of 11.1 kpc (Green & McClure-Griffiths 2011). The maser spots show an *Arched* spatial distribution over 50 mas \times 110 mas, corresponding to 520 au \times 1200 au (figure 14). A single maser spot was detected in the ATCA image (IRAS 18090–1832, Walsh et al. 1998), associ-

ated with the denser of two submillimeter continuum cores known to exist in this region (Walsh et al. 2003).

012.68–00.18. This source, associated with W 33 B, is located at a distance of 2.40 kpc, determined from trigonometric parallax measurements of 22 GHz water masers (Immer et al. 2013). Although the maser spots are roughly distributed along the north-west–south-east direction we classified the morphology of this source as *Complex* (figure 15). The masers are distributed over 130 mas \times 270 mas, corresponding to 310 au \times 650 au. The associated submillimeter continuum emission is extended along the north-east–south-west direction perpendicular to the methanol maser distribution (Walsh et al. 2003).

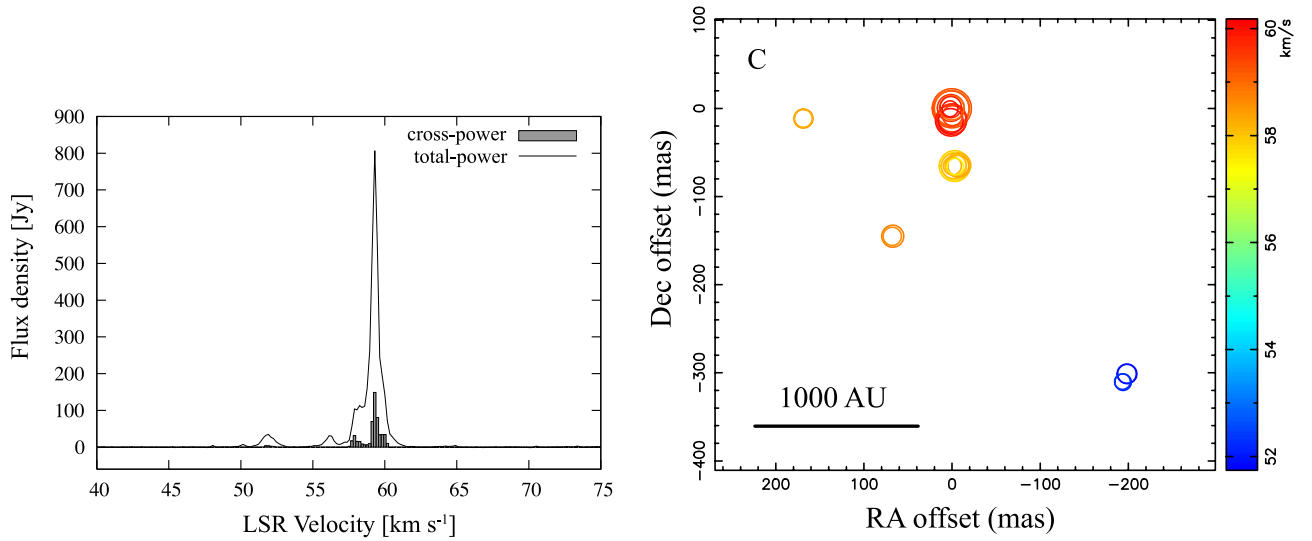


Fig. 30. Data for source 049.49–00.38, plotted the same as in figure 2.

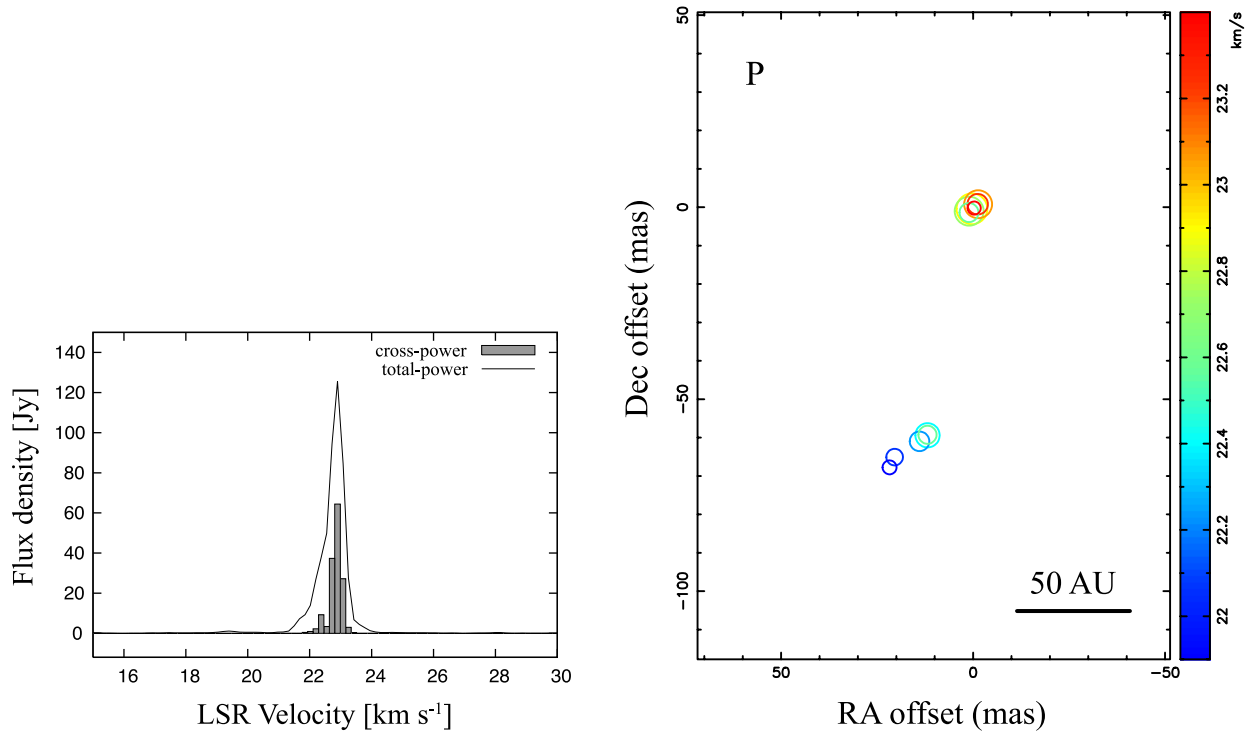


Fig. 31. Data for source 232.62+00.99, plotted the same as in figure 2.

012.88+00.48. This source is located at a trigonometric parallax distance of 2.34 kpc (Xu et al. 2011). The flux of its methanol maser is known to show a periodic variation with a period of 29.5 d (Goedhart et al. 2009). The 6.7 GHz methanol maser spots are comprised of a main cluster and two separated clusters, constituting *Complex* morphology (figure 16). The main cluster is seen in the ATCA image (IRAS 18089–1732, Walsh et al. 1998) as A–E, H, and J. The cluster located at 1''.5 in a north-easterly direction

corresponds to spot F in the ATCA image. While spot G in the ATCA image is absent, EAVN detected new maser spots at 1''.9 north-east from the main cluster, whose $V_{\text{lsr}} = 32.53\text{--}32.88\text{ km s}^{-1}$. Additional new maser spots, with a range of $V_{\text{lsr}} = 34.29\text{--}34.99\text{ km s}^{-1}$, appear around the origin. The masers are distributed over $1100\text{ mas} \times 1600\text{ mas}$, corresponding to $2600\text{ au} \times 3800\text{ au}$.

014.10+00.08. This source is located at a distance of 5.4 kpc (Green & McClure-Griffiths 2011). As mentioned

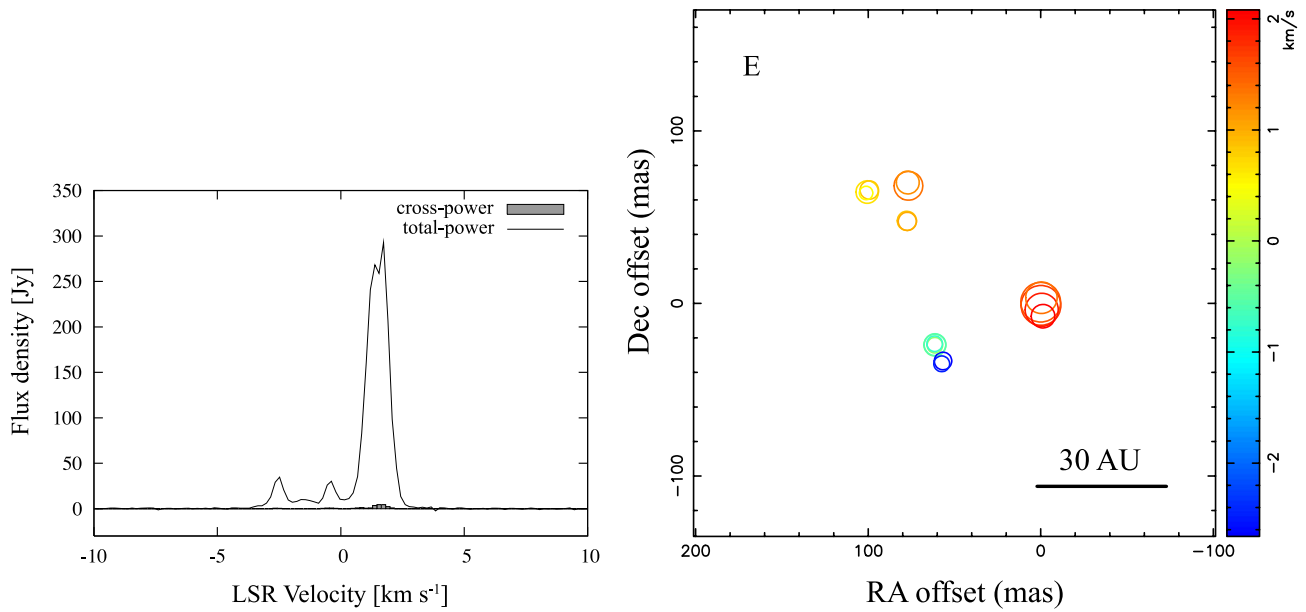


Fig. 32. Data for source 351.77–00.53, plotted the same as in figure 2.

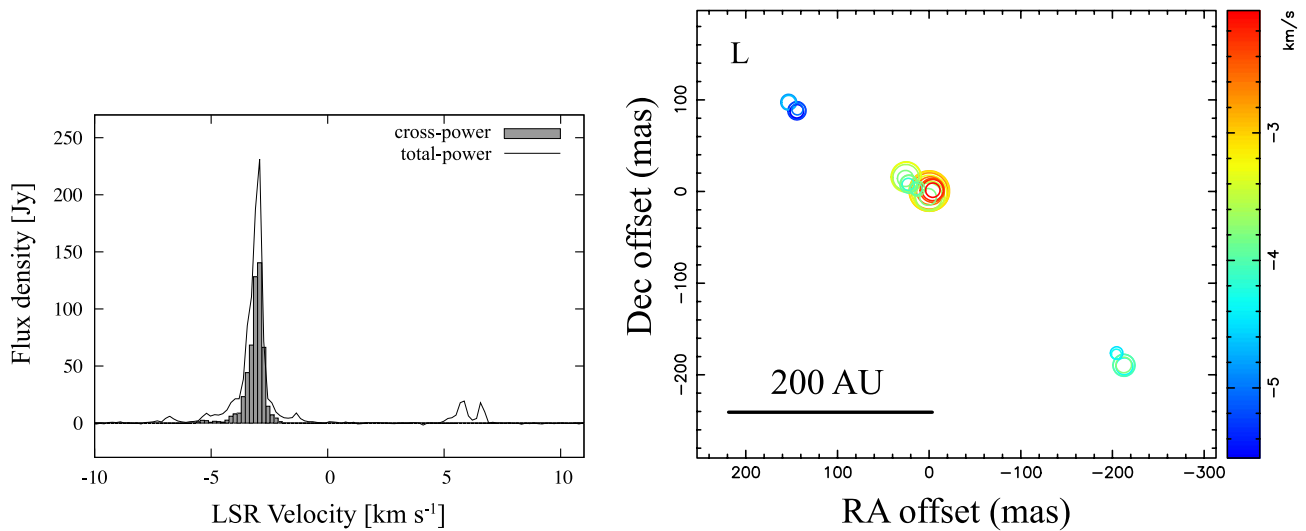


Fig. 33. Data for source 352.63–01.06, plotted the same as in figure 2.

in section 3, 014.10+00.08 was detected only by the short Mizusawa–Hitachi baseline. Therefore, an image of this source was not made.

020.23+00.06. This source is located at a kinematic distance of 4.4 kpc (Green & McClure-Griffiths 2011). Two isolated maser clusters are separated by 8".5 (equivalently, by 3.7×10^4 au, figure 17). The maser spots in each cluster are probably excited by different high-mass YSOs. In the south-western maser cluster (SW), two isolated clusters are separated by 70 mas (320 au) at the source. Therefore, the morphology of this cluster is *Paired*. The velocities of maser spots in the north-eastern maser cluster (NE) vary widely

(by 11 km s⁻¹), although the spatial coverage is only 100 au. The morphology of this cluster is *Arched*.

023.43–00.18. Trigonometric parallax measurements of 12 GHz methanol masers identified this source at a distance of 5.9 kpc (Brunthaler et al. 2009). The masers form two clusters separated by approximately 14", corresponding to 8.2×10^4 au (figure 18). Two millimeter dust continuum cores have been reported to the north (MM1) and south (MM2) of this region (Ren et al. 2011). Each methanol maser cluster is associated with each mm dust core, suggesting that these separated clusters are located in different high-mass star-forming regions. Both maser clusters appear

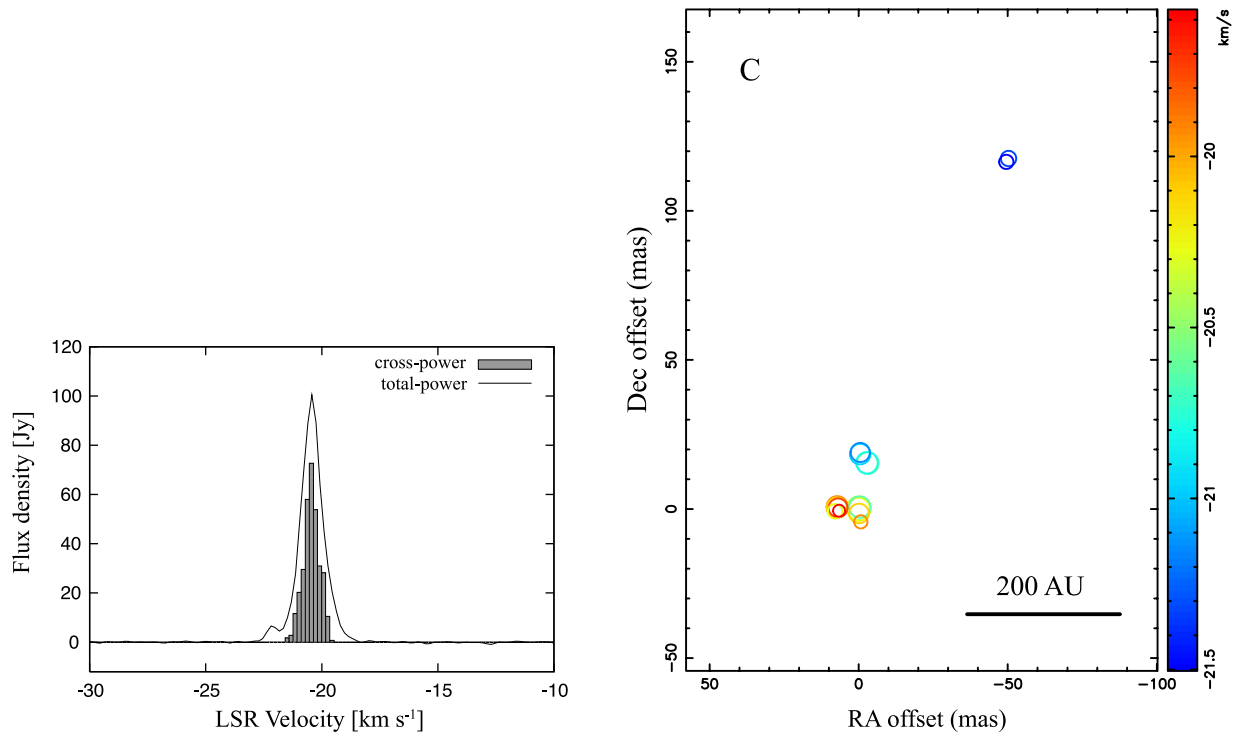


Fig. 34. Data for source 353.41–00.36, plotted the same as in figure 2.

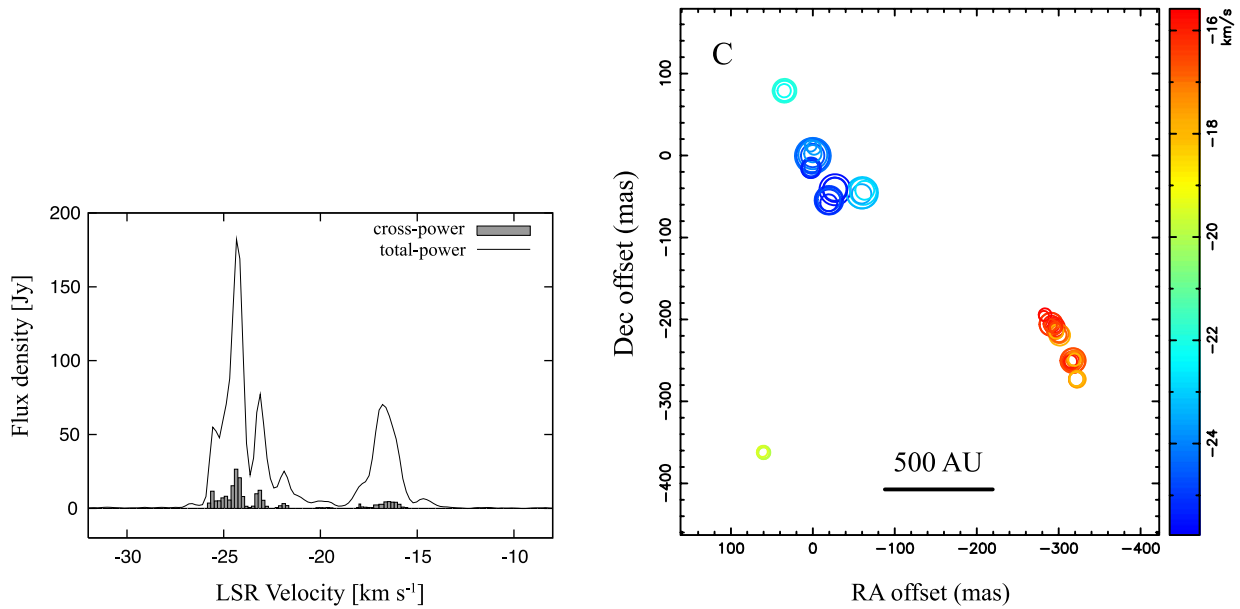


Fig. 35. Data for source 354.61+00.47, plotted the same as in figure 2.

in the ATCA image (IRAS 18319–0834, Walsh et al. 1998). The maser spots in the MM2 and MM1 regions coincide with those labeled C–F and J–L in the ATCA image, respectively. The morphology of the northern cluster MM1 is *Complex*. The maser spots are distributed over $18 \text{ mas} \times 18 \text{ mas}$, corresponding to $110 \text{ au} \times 110 \text{ au}$. The

southern cluster MM2 is *Paired*. The masers in this cluster are distributed over $280 \text{ mas} \times 90 \text{ mas}$ ($1600 \text{ au} \times 550 \text{ au}$). 025.65+01.05. This source is located at a kinematic distance of 12.5 kpc (Green & McClure-Griffiths 2011). The morphology of the methanol maser is *Linear* (figure 19). The masers are distributed over $7 \text{ mas} \times 2 \text{ mas}$,

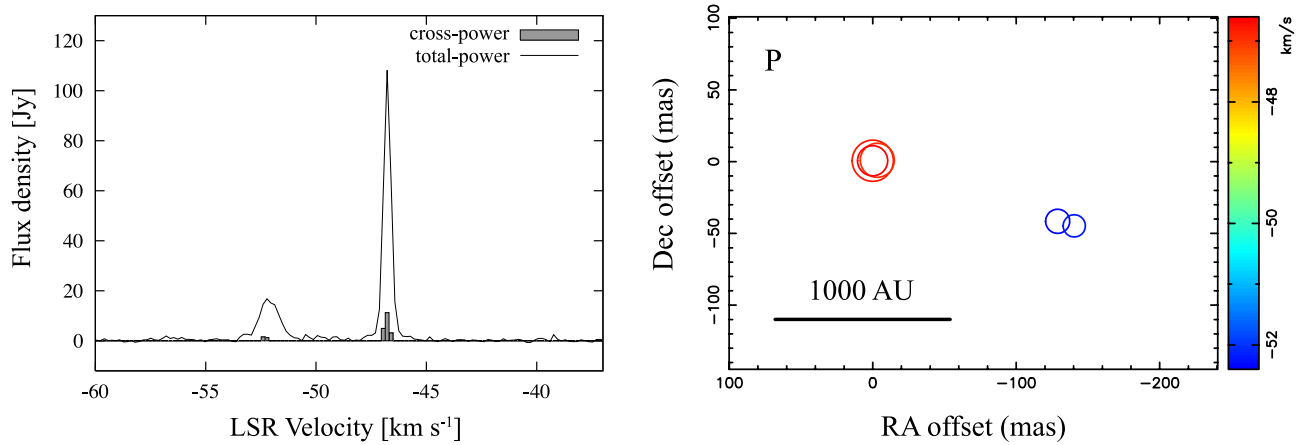


Fig. 36. Data for source 359.43–00.10, plotted the same as in figure 2.

corresponding to $90 \text{ au} \times 20 \text{ au}$. The radial velocity width is quite narrow (less than 1 km s^{-1}). The ATCA image is elongated approximately $1''$ in a north–south direction (IRAS 18316–0602, Walsh et al. 1998). The spots in the VLBI image coincide with spot B in the ATCA image.

025.71+00.04. This source is located at a kinematic distance of 11.8 kpc (Pandian et al. 2008). The morphology is *Complex* (figure 20). The maser spots are distributed over $80 \text{ mas} \times 130 \text{ mas}$, corresponding to $930 \text{ au} \times 1500 \text{ au}$. These spots coincide with those labeled C, D, and J in the ATCA image (IRAS 18353–0628, Walsh et al. 1998).

025.82–00.17. This source is located at a kinematic distance of 5.0 kpc (Green & McClure-Griffiths 2011). The 6.7 GHz methanol maser spots are distributed in *Elliptical* morphology with a clockwise velocity gradient (figure 21). The scale is $300 \text{ mas} \times 300 \text{ mas}$, corresponding to $1500 \text{ au} \times 1500 \text{ au}$ at the source. The EAVN and ATCA images of this source are similarly structured (IRAS 18361–0627, Walsh et al. 1998).

028.83–00.25. This source is located at a kinematic distance of 4.6 kpc (Green & McClure-Griffiths 2011). The spatial distribution is *Arched* (figure 22). The maser spots are distributed over $370 \text{ mas} \times 440 \text{ mas}$, corresponding to $1700 \text{ au} \times 2000 \text{ au}$. These spots coincide with those labeled B, D, and G in the ATCA image (IRAS 18421–0348, Walsh et al. 1998). The EAVN image is similar to the JVLA image presented in Cyganowski et al. (2009).

029.86–00.04. The target source 029.86–00.04 is adjacent ($\sim 7'$) to two H II regions designated G029.95–00.01 and G029.97–00.04. The distances of these H II regions derived from H I SA and the formaldehyde absorption line spectrum are 9.3 and 9.2 kpc, respectively (Anderson & Bania 2009; Downes et al. 1980). Thus, we assume a distance of 9.3 kpc for source 029.86–00.04. The 6.7 GHz methanol maser spots reveal an *Arched* distribution accompanied by a clear

velocity gradient (figure 23). The scale of the distribution is $150 \text{ mas} \times 340 \text{ mas}$, corresponding to $1400 \text{ au} \times 3200 \text{ au}$ at the source.

030.70–00.06. This source is located in a star-forming region known as the W43 main complex (Motte et al. 2003). The masers are associated with the millimeter dust continuum MM2 (Motte et al. 2003), one of the most massive and luminous cores in the complex. Thus, we assume that 030.70–00.06 is located at 5.9 kpc, the measured distance of W 43. The morphology of this source is *Paired* (figure 24). The maser spots are distributed over $690 \text{ mas} \times 420 \text{ mas}$, corresponding to $4100 \text{ au} \times 2500 \text{ au}$. **030.76–00.05.** The kinematic distance of this source is 4.8 kpc (Anderson & Bania 2009). The 6.7 GHz methanol maser spots form two distinct clusters isolated by 34 mas, corresponding to 160 au; therefore, the morphology of this source is *Paired* (figure 25). The maser spots coincide with those labeled D–F in the ATCA image (IRAS 18450–0200, Walsh et al. 1998).

030.91+00.14. This source is located at a kinematic distance of 5.6 kpc (Anderson & Bania 2009). The morphology is *Linear* with a clear continuous velocity gradient (figure 26). The maser spots are distributed over $30 \text{ mas} \times 60 \text{ mas}$, corresponding to $150 \text{ au} \times 320 \text{ au}$, and they are associated with submillimeter continuum emission (Hill et al. 2005).

031.28+00.06. The distance of this source is 5.8 kpc (Anderson & Bania 2009). The 6.7 GHz methanol maser spots form a *Complex* distribution over $560 \text{ mas} \times 470 \text{ mas}$, corresponding to $3300 \text{ au} \times 2700 \text{ au}$ at the source (figure 27). The maser spots in the VLBI image correspond to those labeled A–K in the ATCA image (IRAS 18456–0129, Walsh et al. 1998). A VLBI image of this source was also obtained by EVN (Minier et al. 2000). The overall distributions in the EAVN and EVN

images are closely matched. However, the maser spots at $V_{\text{lsr}} = 109.42$ and 109.87 km s^{-1} in the EVN image are absent in the EAVN image, while new maser spots appear at $V_{\text{lsr}} = 104.34$ and 104.52 km s^{-1} , located at $(\Delta\alpha, \Delta\delta) = (-68, +215)$ from the brightest spot.

032.03+00.06. From the near-IR extinction–distance relationship, the distance of this source has been estimated to be 7.2 kpc (Stead & Hoare 2010). The morphology of this source is *Paired* (figure 28). The maser spots are distributed over $290 \text{ mas} \times 430 \text{ mas}$, corresponding to $2100 \text{ au} \times 3100 \text{ au}$. The masers are associated with millimeter dust continuum and the $4.5 \mu\text{m}$ extended emission observed by Rathborne, Jackson, and Simon (2006) and Chambers et al. (2009).

037.40+01.52. The kinematic distance of this source is 2.1 kpc (Fontani et al. 2011). The morphology is *Linear* with a clear velocity gradient (figure 29). The maser spots are distributed over $30 \text{ mas} \times 10 \text{ mas}$, corresponding to $60 \text{ au} \times 20 \text{ au}$. The linear spatial distribution, the size, and the velocity gradient are similar to those of NGC 7538 IRS1 with a linear size of 90 au (Minier et al. 1998).

049.49–00.38. This source is located in the well-known complex high-mass star-forming region W 51. From two reported trigonometric parallax distances, namely $5.1^{+2.9}_{-1.4}$ (Xu et al. 2009a) and $5.41^{+0.31}_{-0.28}$ (Sato et al. 2010), we assign a distance of 5.41 kpc to 049.49–00.38. Maser emissions have been reported at several sites within an area of $2'$, enclosing W 51 Main and IRS2, but here we concentrate on the target source 049.49–00.38 in W 51 Main. The 6.7 GHz methanol maser spots are distributed in *Complex* morphology over $370 \text{ mas} \times 310 \text{ mas}$, corresponding to $2000 \text{ au} \times 1700 \text{ au}$ at the source (figure 30). From MERLIN data, Etoaka, Gray, and Fuller (2012) showed that the 6.7 GHz methanol maser spots of this source are distributed over an area of $3'' \times 2''$. The southern spots detected by MERLIN were absent in the EAVN image. The distribution of maser spots of this source was also obtained by EVN (Phillips & van Langevelde 2005; Surcis et al. 2012) and found to be consistent with that in the EAVN image.

232.62+00.99. This source is located at a distance of 1.68 kpc, estimated from trigonometric parallax measurements of the 12 GHz methanol maser (Reid et al. 2009). The morphology of this source is *Paired* (figure 31). The maser spots are distributed over $20 \text{ mas} \times 70 \text{ mas}$, corresponding to $40 \text{ au} \times 120 \text{ au}$. These spots coincide with the spots labeled B and C in the ATCA image (IRAS 07299–1651, Walsh et al. 1998).

351.77–00.53. The distance of this source is 0.4 kpc with a large uncertainty (Green & McClure-Griffiths 2011). The morphology of this source is *Elliptical* (although the southwestern section is missing in the image) with a clockwise velocity gradient (figure 32). The maser spots are distributed

over $100 \text{ mas} \times 100 \text{ mas}$ ($40 \text{ au} \times 40 \text{ au}$) and coincide with those labeled A–D in the ATCA image (IRAS 17233–3606, Walsh et al. 1998). A strong ^{12}CO bipolar outflow and OH maser outflow have been reported in this region (Leurini et al. 2008).

352.63–01.06. This source is located at a kinematic distance of 0.9 kpc, with a large uncertainty (Green & McClure-Griffiths 2011). The morphology is *Linear*, but the velocity distribution is complex (figure 33). The maser spots are distributed over $370 \text{ mas} \times 290 \text{ mas}$, corresponding to $330 \text{ au} \times 260 \text{ au}$. These maser spots coincide with those labeled D and F in the ATCA image (IRAS 17278–3541, Walsh et al. 1998). New maser spots are detected at $(\Delta\alpha, \Delta\delta) = (-210, -190)$ from the brightest maser spot. The 6.7 GHz methanol masers are located at a peak of the 1.2 mm dust continuum emission (Faúndez et al. 2004).

353.41–00.36. The kinematic distance of this source is 3.8 kpc (Caswell et al. 2011). The morphology is *Complex* (figure 34). The maser spots are distributed over $60 \text{ mas} \times 120 \text{ mas}$, corresponding to $220 \text{ au} \times 460 \text{ au}$, and they coincide with those labeled A–C in the ATCA image (IRAS 17271–3439, Walsh et al. 1998). The 6.7 GHz methanol maser is associated with a peak of the millimeter dust continuum and centimeter radio continuum sources (Garay et al. 2006, 2007). From radio continuum observations, the exciting star is thought to be of spectral type O9.5. The SiO and CH_3CCH lines have also been detected in this region (Miettinen et al. 2006).

354.61+00.47. This source is located at a kinematic distance of 3.8 kpc (Green & McClure-Griffiths 2011). The morphology is *Complex*, formed by three clusters (figure 35). The scale of the maser distribution is $380 \text{ mas} \times 440 \text{ mas}$, corresponding to $1500 \text{ au} \times 1700 \text{ au}$. The 6.7 GHz methanol masers are located close to a peak of the millimeter dust continuum emission (Faúndez et al. 2004).

359.43–00.10. This maser source is located at a kinematic distance of 8.2 kpc, and the apparent position is approximately $1'$ east of Sgr C (Fish et al. 2003). The morphology is *Paired* (figure 36). The maser spots are distributed over $140 \text{ mas} \times 50 \text{ mas}$, corresponding to $1200 \text{ au} \times 370 \text{ au}$.

5 Discussions

5.1 Spatial distribution of maser emissions

The distributions of the 6.7 GHz methanol maser spots vary widely in size and structure, similar to the results of previous studies by Bartkiewicz et al. (2009) and Pandian et al. (2011). The whole sizes of the spatial distribution vary from 9 to 4900 au. The 6.7 GHz methanol maser is excited by infrared radiation when its dust temperature is 100–200 K

(Cragg et al. 2005). The spatial scale of the maser distribution can be estimated from the luminosity of the emitting source. Assuming a luminosity from 10^3 to $10^5 L_{\odot}$ and a suitable dust temperature of 100 K, the maser is predicted to appear at 500–5000 au from the excited star, consistent with the observation.

On the other hand, the maser distributions of some sources deviate from their expected range. The three sources, 000.54–00.85 NW/SE, 020.23+00.06 SW/NE, and 023.43–00.18 MM1/2, cannot be attributed to excitation of a single central source having luminosities from 10^3 to $10^5 L_{\odot}$, because the separation of their masers exceeds 10^4 au, indicating that each source likely involves at least two exciting sources. In the following discussion, we assume that these largely separated clusters are associated with individual exciting sources; that is, these are independent sources. Hence we use 38 as a number of the imaged sources, hereafter.

The spatial scale of the maser distribution is plotted as a function of observed radial velocity range in figure 37. The spatial scale of each source is defined as the largest extent of spot distribution in the celestial sphere, while the velocity range is the difference between the smallest and largest velocities of the maser spots detected by VLBI (see table 3). Open circles denote sources with *Linear* morphology, and the filled circles represent other morphological types (*Elliptical*, *Arched*, *Paired*, and *Complex*). A positive correlation is observed between the spatial scale and the radial velocity range, as previously reported by Pandian et al. (2011). Note, however, that sources of *Linear* morphology are the main contributors to this correlation. The spatial distribution of all *Linearly* distributed sources is below 600 au, and their radial velocity range is smaller than 4 km s^{-1} , below those of other sources. If the *Linearly* distributed sources are excluded from figure 37, the correlation between size and radial velocity range becomes much weaker. This tendency toward small radial velocity range

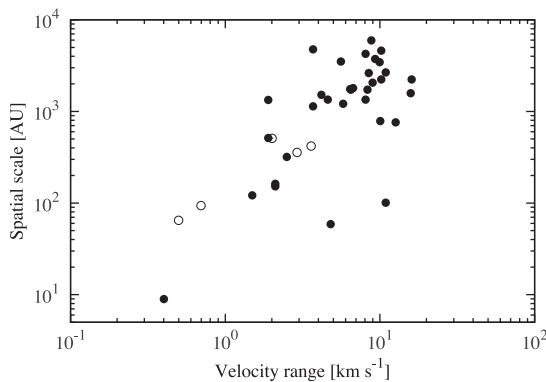


Fig. 37. Spatial scale of maser distribution as a function of velocity range. The open circles indicate sources with *Linear* morphology (see text for details).

Table 4. Spatial morphology of EAVN and EVN samples.*

Array	Spatial Morphology				
	Elliptical†	Arched	Linear	Paired	Complex
EAVN	6	4	5	8	15
(%)	(16)	(11)	(13)	(21)	(39)
EVN	9	3	5	1	9
(%)	(33)	(11)	(19)	(4)	(33)

*The EVN data are taken from Bartkiewicz et al. (2009). Note that 27 sources, classified into the five morphological types, are included in this table.

†“Elliptical” is defined as “Ring” in Bartkiewicz et al. (2009).

and spatial extent in sources of *Linear* distribution has been similarly seen in the results of Pandian et al. (2011). As discussed in the following subsection, we consider that sources of such a restricted size and velocity range are the observable parts of larger structures that are not completely revealed.

5.2 Morphology and the spreading structure of each source

Table 4 summarizes the number of sources satisfying each morphology, as the number of sources and as a fraction of the total number of sources. For comparison, 27 sources observed by EVN and classified into the five types are also listed (these have previously been reported in Bartkiewicz et al. 2009). The number of *Elliptical* sources, which is expected to trace the gas disk around YSOs, is six (16%), small as compared with that (33%) in Bartkiewicz et al. (2009). Our samples contain relatively high numbers of *Paired* (21%) and *Complex* (39%) distributions, which contain no apparent systematic spatial distribution.

Since structures of low intensity are not detected by VLBI, sources with *Paired* or *Complex* morphology may in fact possess low-brightness *Elliptical*, or other systematic, structures. The ratio of the integrated flux of CLEAN components to the total flux is listed in table 3. To investigate the fraction of maser radiation detectable by VLBI, a histogram of these ratios is presented in figure 38. The detectability is from 1% to 58%, averaging around 20%. Similarly, Bartkiewicz et al. (2009) noted that, for most sources, 10%–30% of the total flux were detected by EVN. Our result suggests that 80% of the maser emissions spread spatially into a diffuse structure. Distribution of total-power versus correlated flux is shown in figure 39 with a different symbol for each morphology. This is for testing whether detectability differs with the morphology, but no clear tendency of distribution is seen for different morphology.

Minier, Booth, and Conway (2002) mentioned that some of 6.7 GHz methanol maser emissions consist of compact core and spreading halos whose sizes are a few (tens of)

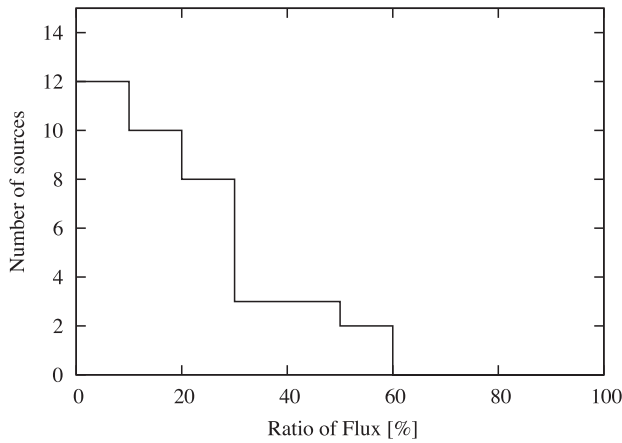


Fig. 38. Histogram of the flux ratio of the correlated to the total-power spectrum. Bins on the horizontal axis are separated by 10%.

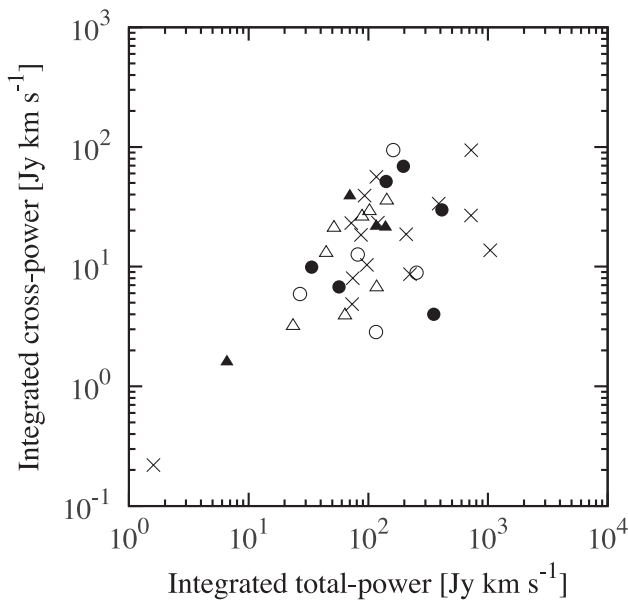


Fig. 39. Distribution of total-power versus correlated flux. Different symbols denote each morphology: filled circles indicate sources with *Elliptical* morphology; open circles are *Linear*; filled triangles are *Arched*; open triangles are *Paired*; crosses are *Complex*.

astronomical units and a few hundred or larger astronomical units, respectively. Pandian et al. (2011) also reported that some maser spots possess no compact core. The spatial distribution of such dispersed maser emissions cannot be determined by VLBI observation. Therefore, as discussed for the *Linearly* distributed sources, we consider that it is difficult to deduce the exact spatial distribution or morphological class of maser emissions from VLBI observations alone.

When interpreting the proper motion of the maser spot and its associated site, any non observed parts must be identified. To avoid the resolved-out problem, the diffuse structure should be observed. Assuming that the emission component spreads into a halo with a size of 300 au, and

that the distance to the source is 3 kpc, the angular size of the spread emission is $0''.1$. To detect this structure, an interferometric observation of spatial resolution approximately $\geq 1''$ is required. We have observed 24 sources among the sources in our sample by ATCA, whose typical spatial resolution is $2''.0 \times 1''.5$. The observed images, which contain the whole emission of the 6.7 GHz masers, will assist in interpreting the VLBI image and obtaining the internal proper motion of the maser spots. The ATCA results will be published elsewhere. High-resolution observations by ALMA will be important for determining the gas and dust distributions within the sources. In future studies, these distributions will be able to be compared with the distribution of the masers.

5.3 Future prospect for proper motion measurements

Despite being limited by the resolved-out problem, VLBI detects 1%–58% of the maser emission, implying that the emission is concentrated in sufficiently compact spots. The number of detected spots in each source is from 3 to 72, with an average of 29. In 34 out of the sources, the spot number is larger than, or equal to, 10, which is sufficient for investigating the three-dimensional velocity field. The relatively long lifetime of the 6.7 GHz maser spot (Goedhart et al. 2004; Ellingsen 2007) has enabled us to observe spots at three epochs over two years. The relative position of the maser spot in each map was measured with an accuracy higher than 0.1 mas, although in practice the accuracy depends on the signal-to-noise ratio of each component. Three repeats of this monitoring observation, planned over two years, will allow us to determine the internal proper motion to an accuracy of $1\sigma = 0.03 \text{ mas yr}^{-1}$. At a typical distance of 3 kpc, this accuracy of proper motion corresponds to a tangential velocity of 1.5 km s^{-1} . Since the average radial velocity width of the maser is 6.5 km s^{-1} , the internal proper motion is detectable at sufficiently high signal-to-noise ratio. In fact, from these previous JVN observations, we measured the internal proper motions of the spots for four sources (Matsumoto et al. 2011; Sugiyama et al. 2011, 2013; Sawada-Satoh et al. 2013).

6 Conclusion

To study the associated site of the 6.7 GHz methanol maser and the gas dynamics around high-mass YSOs, we have monitored the internal proper motion of the maser. For the purpose, 36 selected sources were studied by using multi-epoch VLBI observations of EAVN. We present 35 VLBI

images successfully obtained from the first epoch observation. Three sources contain two separated star-forming regions in each image, yielding 38 imaged sources. The distribution of the detected maser spots was from 9 to 4900 au and displayed the range of morphology. The flux detected by VLBI was 1%–58% of the total flux, suggesting that a large fraction of the radiation is dispersed into an extended structure invisible to VLBI. To investigate the associated site and motion of the maser, shorter baselines are required to recover the distribution of this extended emission. In 34 imaged sources out of 38, we detected 10 or more spots. The accuracy of the spot position was approximately 0.1 mas. Therefore, the internal proper motions could be measured with sufficient accuracy following two years of monitoring observation. From these results, we can statistically investigate the three-dimensional velocity field around high-mass YSOs. Since most of the observed sources are located in the southern hemisphere, they can be observed with the Atacama Large Millimeter/Submillimeter Array (ALMA) in future.

Acknowledgments

The authors wish to thank the JVN team for observational assistance and support. The JVN project is led by the National Astronomical Observatory of Japan (NAOJ), which is a branch of the National Institutes of Natural Sciences (NINS), Hokkaido University, Ibaraki University, University of Tsukuba, Gifu University, Osaka Prefecture University, Yamaguchi University, and Kagoshima University, in cooperation with the Geospatial Information Authority of Japan (GSI), the Japan Aerospace Exploration Agency (JAXA), and the National Institute of Information and Communications Technology (NICT). This work was financially supported in part by a Grant-in-Aid for Scientific Research (KAKENHI) from Japan Society for the Promotion of Science (JSPS), No. 24340034. This work is partly supported by China Ministry of Science and Technology under State Key Development Program for Basic Research (2012CB821800), the National Natural Science Foundation of China (grants 10625314, 11121062, and 11173046), the CAS/SAFEA International Partnership Program for Creative Research Teams, and the Strategic Priority Research Program on Space Science, the Chinese Academy of Sciences (Grant No. XDA04060700).

APPENDIX. Spatial distribution in unified scale

VLBI images of 38 sources are shown in figures 40–77, which are available only in the online version¹ in the same spatial scale (5310 au in both RA and Dec) for all sources. These figures correspond to figures 2–36 in the main text. A 500 au scale bar and the spectrum are shown in the corner of each figure.

¹ (<http://dx.doi.org/10.1093/pasj/psu015>).

Supporting information

Additional Supporting Information may be found in the online version of this article:

Figures 40–77

Please note: Oxford University Press are not responsible for the content or functionality of any supporting materials supplied by the authors. Any queries (other than missing material) should be directed to the corresponding author for the article.

References

- Anderson, L. D., & Bania, T. M. 2009, *ApJ*, 690, 706
- Bartkiewicz, A., Szymczak, M., van Langevelde, H. J., Richards, A. M. S., & Pihlström, Y. M. 2009, *A&A*, 502, 155
- Brunthaler, A., Reid, M. J., Menten, K. M., Zheng, X. W., Moscadelli, L., & Xu, Y. 2009, *ApJ*, 693, 424
- Caswell, J. L. 2009, *PASA*, 26, 454
- Caswell, J. L., et al. 2010, *MNRAS*, 404, 1029
- Caswell, J. L., et al. 2011, *MNRAS*, 417, 1964
- Caswell, J. L., Vaile, R. A., Ellingsen, S. P., & Norris, R. P. 1995, *MNRAS*, 274, 1126
- Chambers, E. T., Jackson, J. M., Rathborne, J. M., & Simon, R. 2009, *ApJS*, 181, 360
- Cragg, D. M., Sobolev, A. M., & Godfrey, P. D. 2005, *MNRAS*, 360, 533
- Cyganowski, C. J., Brogan, C. L., Hunter, T. R., & Churchwell, E. 2009, *ApJ*, 702, 1615
- Dame, T. M., & Thaddeus, P. 2008, *ApJ*, 683, L143
- De Buizer, J. M. 2003, *MNRAS*, 341, 277
- De Buizer, J. M., Redman, R. O., Longmore, S. N., Caswell, J., & Feldman, P. A. 2009, *A&A*, 493, 127
- Dodson, R., Ojha, R., & Ellingsen, S. P. 2004, *MNRAS*, 351, 779
- Doi, A., et al. 2006, *Proc. of the 8th European VLBI Network Symp.*, ed. B. Willem et al. *PoS(8thEVN) (Trieste: SISSA)*, 071
- Downes, D., Wilson, T. L., Bieging, J., & Wink, J. 1980, *A&AS*, 40, 379
- Ellingsen, S. P. 2007, *MNRAS*, 377, 571
- Etoka, S., Gray, M. D., & Fuller, G. A. 2012, *MNRAS*, 423, 647
- Faúndez, S., Bronfman, L., Garay, G., Chini, R., Nyman, L.-Å., & May, J. 2004, *A&A*, 426, 97
- Fish, V. L., Reid, M. J., Wilner, D. J., & Churchwell, E. 2003, *ApJ*, 587, 701
- Fontani, F., et al. 2011, *A&A*, 529, L7
- Fujisawa, K., Mashiyama, H., Shimoikura, T., & Kawaguchi, N. 2002, in *Proc. IAU 8th Asian-Pacific Regional Meeting, Volume II*, ed. S. Ikeuchi et al. (Tokyo: Astronomical Society of Japan), 3
- Garay, G., Brooks, K. J., Mardones, D., & Norris, R. P. 2006, *ApJ*, 651, 914
- Garay, G., Mardones, D., Brooks, K. J., Videla, L., & Contreras, Y. 2007, *ApJ*, 666, 309
- Garay, G., Rodríguez, L. F., Moran, J. M., & Churchwell, E. 1993, *ApJ*, 418, 368
- Goddi, C., Moscadelli, L., & Sanna, A. 2011, *A&A*, 535, L8

- Goedhart, S., Gaylard, M. J., & van der Walt, D. J. 2004, *MNRAS*, 355, 553
- Goedhart, S., Langa, M. C., Gaylard, M. J., & van der Walt, D. J. 2009, *MNRAS*, 398, 995
- Green, J. A., et al. 2010, *MNRAS*, 409, 913
- Green, J. A., et al. 2012, *MNRAS*, 420, 3108
- Green, J. A., & McClure-Griffiths, N. M. 2011, *MNRAS*, 417, 2500
- Greisen, E. W. 2003, in *Information Handling in Astronomy – Historical Vistas*, ed. A. Heck (Dordrecht: Kluwer Academic Publisher), 109
- Hill, T., Burton, M. G., Minier, V., Thompson, M. A., Walsh, A. J., Hunt-Cunningham, M., & Garay, G. 2005, *MNRAS*, 363, 405
- Immer, K., Reid, M. J., Menten, K. M., Brunthaler, A., & Dame, T. M. 2013, *A&A*, 553, A117
- Kurtz, S., & Franco, J. 2002, *Rev. Mex. Astron. Astrofis., Ser. Conf.*, 12, 16
- Laurini, S., Hieret, C., Thorwirth, S., Wyrowski, F., Schilke, P., Menten, K. M., Güsten, R., & Zapata, L. 2008, *A&A*, 485, 167
- Longmore, S. N., Pillai, T., Keto, E., Zhang, Q., & Qiu, K. 2011, *ApJ*, 726, 97
- Matsumoto, N., et al. 2011, *PASJ*, 63, 1345
- Menten, K. M. 1991, *ApJ*, 380, L75
- Miettinen, O., Harju, J., Haikala, L. K., & Pomrén, C. 2006, *A&A*, 460, 721
- Minh, Y. C., Roh, D.-G., Han, S.-T., & Kim, H.-G. 2003, in *ASP Conf. Ser.*, 306, *New Technologies in VLBI*, ed. Y. C. Minh (San Francisco: ASP), 373
- Minier, V., Booth, R. S., & Conway, J. E. 1998, *A&A*, 336, L5
- Minier, V., Booth, R. S., & Conway, J. E. 2000, *A&A*, 362, 1093
- Minier, V., Booth, R. S., & Conway, J. E. 2002, *A&A*, 383, 614
- Minier, V., Ellingsen, S. P., Norris, R. P., & Booth, R. S. 2003, *A&A*, 403, 1095
- Moisés, A. P., Damini, A., Figuerêdo, E., Blum, R. D., Conti, P. S., & Barbosa, C. L. 2011, *MNRAS*, 411, 705
- Moscadelli, L., Cesaroni, R., Rioja, M. J., Dodson, R., & Reid, M. J. 2011, *A&A*, 526, A66
- Motte, F., Schilke, P., & Lis, D. C. 2003, *ApJ*, 582, 277
- Nicholas, B., Rowell, G., Burton, M. G., Walsh, A., Fukui, Y., Kawamura, A., Longmore, S., & Keto, E. 2011, *MNRAS*, 411, 1367
- Norris, R. P., Whiteoak, J. B., Caswell, J. L., Wieringa, M. H., & Gough, R. G. 1993, *ApJ*, 412, 222
- Pandian, J. D., Goldsmith, P. F., & Deshpande, A. A. 2007, *ApJ*, 656, 255
- Pandian, J. D., Momjian, E., & Goldsmith, P. F. 2008, *A&A*, 486, 191
- Pandian, J. D., Momjian, E., Xu, Y., Menten, K. M., & Goldsmith, P. F. 2011, *ApJ*, 730, 55
- Pestalozzi, M. R., Minier, V., & Booth, R. S. 2005, *A&A*, 432, 737
- Phillips, C. J., Norris, R. P., Ellingsen, S. P., & McCulloch, P. M. 1998, *MNRAS*, 300, 1131
- Phillips, C., & van Langevelde, H. J. 2005, in *ASP Conf. Ser.*, 340, *Future Directions in High Resolution Astronomy: The 10th Anniversary of the VLBA*, ed. J. D. Romney & M. J. Reid (San Francisco: ASP), 342
- Rathborne, J. M., Jackson, J. M., & Simon, R. 2006, *ApJ*, 641, 389
- Reid, M. J., Menten, K. M., Zheng, X. W., Brunthaler, A., & Xu, Y. 2009, *ApJ*, 705, 1548
- Ren, J. Z., Liu, T., Wu, Y., & Li, L. 2011, *MNRAS*, 415, L49
- Ren, Z., Wu, Y., Zhu, M., Liu, T., Peng, R., Qin, S., & Li, L. 2012, *MNRAS*, 422, 1098
- Rygl, K. L. J., Brunthaler, A., Reid, M. J., Menten, K. M., van Langevelde, H. J., & Xu, Y. 2010, *A&A*, 511, A2
- Sanna, A., Moscadelli, L., Cesaroni, R., Tarchi, A., Furuya, R. S., & Goddi, C. 2010a, *A&A*, 517, A71
- Sanna, A., Moscadelli, L., Cesaroni, R., Tarchi, A., Furuya, R. S., & Goddi, C. 2010b, *A&A*, 517, A78
- Sanna, A., Reid, M. J., Moscadelli, L., Dome, T. M., Menten, K. M., Brunthaler, A., Zheng, X. W., & Xu, Y. 2009, *ApJ*, 706, 464
- Sato, M., Reid, M. J., Brunthaler, A., & Menten, K. M. 2010, *ApJ*, 720, 1055
- Sawada-Satoh, S., Fujisawa, K., Sugiyama, K., Wajima, K., & Honma, M. 2013, *PASJ*, 65, 79
- Shen, Z., Yang, J., Hirabayashi, H., Inoue, M., Kim, H.-G., & Han, S.-T. 2004, *Proc. Asia-Pacific Radio Science Conf.*, ed. T. Keyun & L. Dayong (New York: IEEE), 401
- Shibata, K. M., Kamenoi, S., Inoue, M., & Kobayashi, H. 1998, in *ASP Conf. Ser.*, 144, *IAU Colloq. 164, Radio Emission from Galactic and Extragalactic Compact Sources*, ed. J. A. Zensus et al. (San Francisco: ASP), 413
- Stead, J. J., & Hoare, M. G. 2010, *MNRAS*, 407, 923
- Sugiyama, K., Fujisawa, K., Doi, A., Honma, M., Kobayashi, H., Bushimata, T., Mochizuki, N., & Murata, Y. 2008, *PASJ*, 60, 23
- Sugiyama, K., et al. 2011, *PASJ*, 63, 53
- Sugiyama, K., et al. 2014, *A&A*, 562, A82
- Surcis, G., Vlemmings, W. H. T., van Langevelde, H. J., & Hutawarakorn Kramer, B. 2012, *A&A*, 541, A47
- Walsh, A. J., Burton, M. G., Hyland, A. R., & Robinson, G. 1998, *MNRAS*, 301, 640
- Walsh, A. J., Macdonald, G. H., Alvey, N. D. S., Burton, M. G., & Lee, J.-K. 2003, *A&A*, 410, 597
- Xu, Y., Li, J. J., Hachisuka, K., Pandian, J. D., Menten, K. M., & Henkel, C. 2008, *A&A*, 485, 729
- Xu, Y., Moscadelli, L., Reid, M. J., Menten, K. M., Zhang, B., Zhang, X. W., & Brunthaler, A. 2011, *ApJ*, 733, 25
- Xu, Y., Reid, M. J., Menten, K. M., Brunthaler, A., Zheng, X. W., & Moscadelli, L. 2009a, *ApJ*, 693, 413
- Xu, Y., Voronkov, M. A., Pandian, J. D., Li, J. J., Sobolev, A. M., Brunthaler, A., Ritter, B., & Menten, K. M. 2009b, *A&A*, 507, 1117
- Ye, S., Wan, T., & Qian, Z. 1991, in *ASP Conf. Ser.*, 19, *IAU Colloq. 131, Radio Interferometry: Theory, Techniques and Applications*, ed. T. J. Cornwell & R. A. Perley (San Francisco: ASP), 386
- Yonekura, Y., et al. 2013, in *New Trends in Radio Astronomy in the ALMA Era*, ed. R. Kawabe et al. (San Francisco: ASP), 415
- Zinnecker, H., & Yorke, H. W. 2007, *ARA&A*, 45, 481